Fall 12-2023

Kinematic Vorticity and Porphyroclast Rotation in Mylonites of the Norumbega Fault System: Implications for Paleoviscometry

Hendrik Lenferink
University of Maine - Main, hendrik.lenferink@maine.edu

KINEMATIC VORTICITY AND PORPHYROCLAST ROTATION IN MYLONITES OF THE NORUMBEGA FAULT SYSTEM: IMPLICATIONS FOR PALEOVISCOMETRY

by

Hendrik J. Lenferink

A Thesis Submitted in Partial Fulfillment
of the Requirements for a Degree with Honors
(Earth Sciences and Physics)

The Honors College

University of Maine

August 2008

Advisory Committee:

Scott E. Johnson, Professor of Earth Sciences
Peter O. Koons, Professor of Earth Sciences
Daniel R. Lux, Professor of Earth Sciences
Samuel T. Hess, Assistant Professor of Physics
Robert A. Brinkley, Associate Professor of English, Honors College

ABSTRACT

Crystallographic and shape preferred orientation (SPO) fabrics that develop in mylonitic shear zones can preserve the mean kinematic vorticity number (W_m) of bulk flow. Microstructural methods exploiting dynamically recrystallized quartz and porphyroclast SPO fabrics typically yield conflicting values of W_m. The Sandhill Corner Mylonite Zone of the Norumbega Fault System, Maine, USA, serves as a case study for investigating this discrepancy; W_m estimates range from 0.90 to 1.00 employing the former method (Method 1) and from 0.3 to 0.6 employing the latter method (Method 2). Using a numerical model, I show how a low-viscosity layer (LVL) surrounding clasts affects their SPO and makes Method 2 underestimate W_m. I propose a method based on my modeling results for estimating the viscosity contrast $\tilde{\eta}$ between the LVL and rock matrix in natural examples.

ACKNOWLEDGEMENTS

Many thanks to Scott Johnson for meeting with me regularly and providing resources and facilities; to Nancy Price for preparing samples and providing quartz c-axis data; to my committee members for their input and criticisms; to my family and friends for all their love and support.

TABLE OF CONTENTS

Introduction

The progressive cooling of Earth gives rise to temperature and density gradients that drive mantle convection. The outer 100 km of Earth forms a conductive thermal boundary layer called the lithosphere, which is partitioned into plates that move around on Earth's surface in response to mantle convection (Fig. 1). Interaction of lithospheric plates leads to deformation at their boundaries in zones of localized flow called shear zones (Fig. 2) as the plates converge, diverge, and slip past one another.

Shear zones and their overlying faults are important subjects of study because they are commonly associated with active seismicity (*e.g.*, the San Andreas Fault System in southern California) that can manifest as earthquakes and endanger human life. Our understanding of deformation in shear zones derives from observations of plate motion and from measurements in rock exhumed from various depths by erosion. The former approach can provide a picture of how present-day deformation is distributed at Earth's surface, but does not offer a means to address deformation far below Earth's surface or during past epochs.

The direction of this thesis follows the latter approach and focuses on microstructural methods called 'kinematic vorticity analyses' used for extracting quantitative information about the kinematics of flow in shear zones. The validity of these methods relies on the assumption that there is perfect coupling between fractured, rigid objects ('porphyroclasts'; Fig. 3) and the stress-supporting viscous medium ('matrix'; Fig. 3) in rocks undergoing ductile deformation; the aim of this work is to test the relaxation of that assumption.

After specifying an appropriate field area for study, two different methods are employed and a discussion follows comparing the results of each. An exploration of possible reasons for discrepancy between the results gives way to new insight regarding the robustness of one method and a new tool for investigating localized deformation at the microstructural scale in shear zones.

But before exploring the different methods of kinematic vorticity analysis and their application to rocks, a description of the environment suitable for their application and a scale for measuring kinematic vorticity are needed.

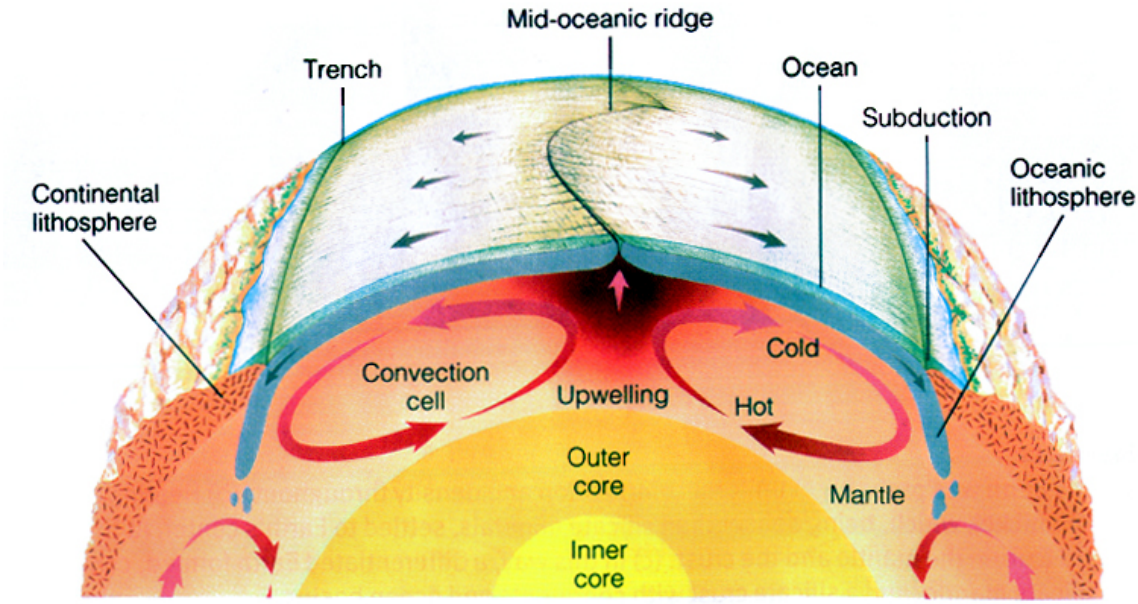

Figure 1: Cross-section of Earth. Arising from density instability, oceanic lithosphere subducts into the convecting mantle, recycling its contents; new lithosphere forms at mid-oceanic spreading ridges. Less dense, continental lithosphere remains atop the convecting mantle. <http://www.yorku.ca/esse/veo/earth/image/1-3-2.jpg>

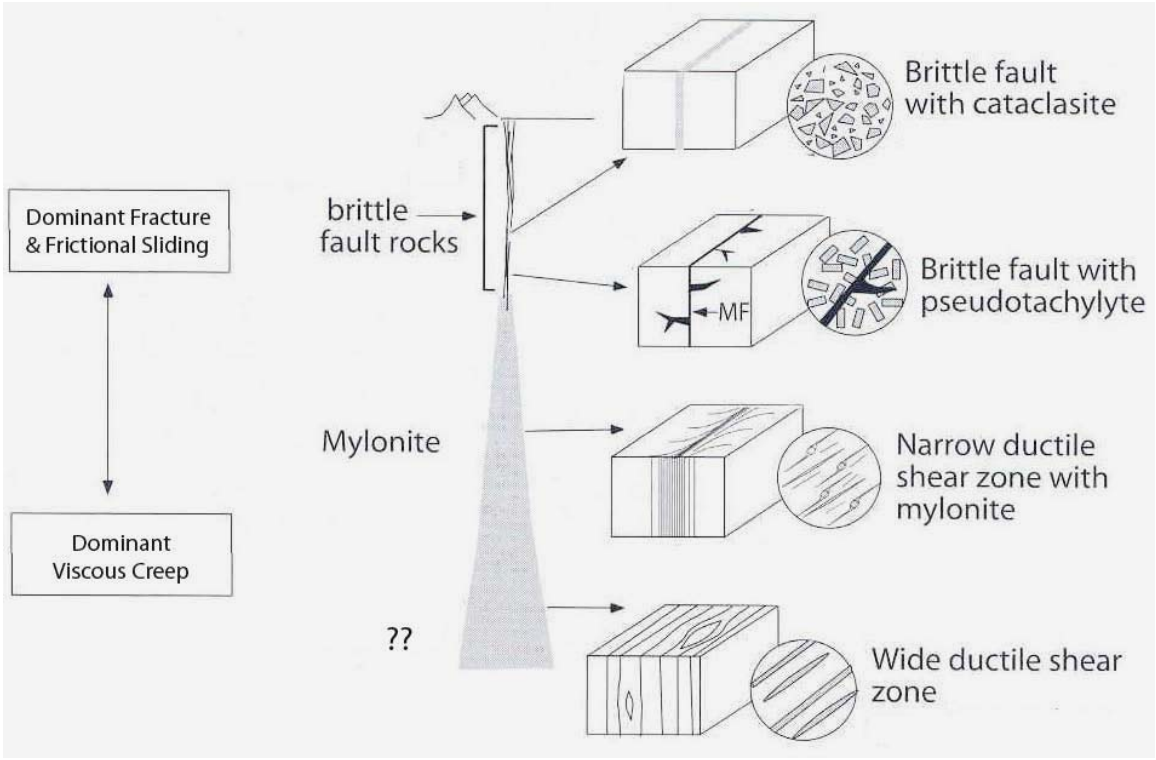

Figure 2: Vertical cross-section of a shear zone and overlying transform fault illustrating the change in structure and rheology with depth. Near the surface, movement is accommodated by fracturing and frictional sliding along discrete faults. Deeper in the crust, frictional melt (pseudotachylyte) can form during slip events due to the frictional heating of rock, recording the maximum penetration depth of earthquakes. At mid-crustal depths the fault transitions into a mylonite zone that deforms as a continuum due to the onset of

quartz plasticity. Overlapping pseudotachylyte and mylonite occurs in the frictional-to-viscous transition zone, below which no earthquakes can penetrate. Image from Passchier and Trouw (2005).

Background

1. *Mylonite zones*

Kinematic vorticity analyses rely on geometric trends in the internal structure ('fabric') of deformed rock. A basic requirement for their application is that the rock underwent monoclinic (defined below) ductile deformation and accumulated large finite strain, resulting in a planar shape fabric ('foliation'; Fig. 3) defined by layering of flat minerals and a linear shape fabric ('lineation') defined by parallel elongate minerals.

Foliated and lineated rocks called mylonites develop at mid-crustal depths in shear zones (Fig. 2) at temperatures above the onset of quartz plasticity and below the onset of feldspar plasticity (400 – 500 ºC). 'Mylonite zones' accommodate most of the deformation in this regime of shear zones and range from mm-scale to km-scale. The intensity of deformation varies among mylonite zones but is always very large (Passchier and Trouw, 2005).

Mylonites can contain relatively large (mm- to cm-scale) mineral fragments (herein interchangeably referred to as porphyroclasts, clasts, particles, and inclusions; Fig. 3 and 8) in an otherwise fine-grained crystalline matrix. Feldspar porphyroclasts develop in quartzo-feldspathic mylonites as more competent parts of the rock continually fragment into clasts which are effectively rigid compared to the viscously-deforming, stress-supporting matrix. By this 'milling' process, originally thought to be the dominant deformation mechanism in these rocks (Lapworth, 1885), mylonites derive their name from the Greek 'μυλων' (mill) (Passchier and Trouw, 2005).

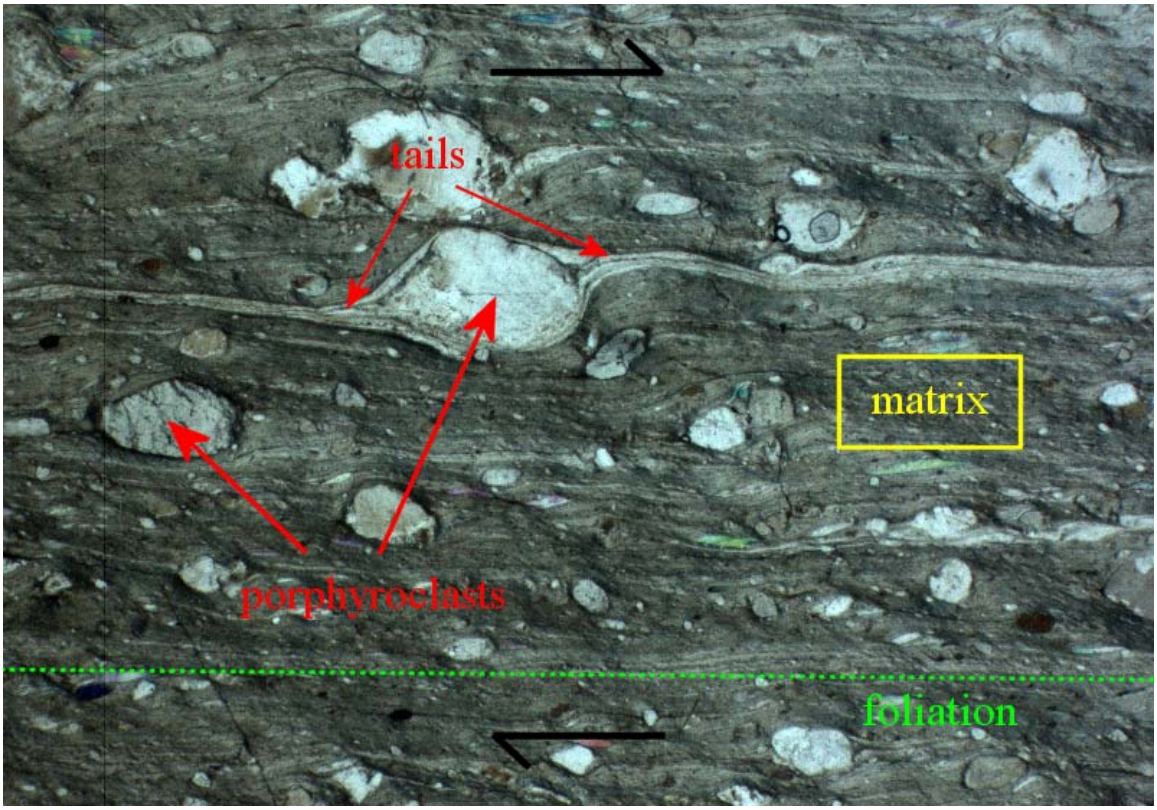

Figure 3: Photomicrograph of a mylonite section parallel to lineation and perpendicular to foliation. Black arrows indicate top-to-the-right sense of shear, as in Fig. 4. Green dotted line represents the trace of the foliation (line of intersection between the foliation plane and image plane, parallel to the lineation). Several feldspar porphyroclasts are present in this sample (white to gray objects). One clast has tails of fine recrystallized material (consisting mainly of quartz) that stretched out into the matrix with progressive deformation.

2. *Kinematic vorticity number* (W_k)

The kinematic vorticity number (W_k) first appeared in fluid dynamics literature (Truesdell, 1953) and was later introduced into geological literature by McKenzie (1979) and Means *et al.* (1980). W_k is a measure of the non-coaxiality of flow, denoting the relative rates of rotation and stretching at a point in space and moment in time (see Appendix 1). Flow types range from pure shear ($W_k = 0$) to simple shear ($W_k = 1$); intermediate types fall under the category of general non-coaxial flow ($0 < W_k < 1$). An alternative measure of non-coaxiality is $s_r = \dot{\varepsilon} / \dot{\gamma}$, the ratio of the rate of pure shearing to the rate of simple shearing (see Appendix 1).

For monoclinic (*i.e.*, rotation in plane containing instantaneous stretching axes ISA_1 and ISA_2 in Fig. 4), plane-strain (*i.e.*, 2-D) deformation, W_k is a function of the acute angle α between the non-vanishing velocity field eigenvectors ('flow apophyses' AP_1 and AP_2 in Fig. 4; see Appendix 2) in the plane containing ISA_1 and ISA_2:

$$W_k = \cos(\alpha) \qquad (1)$$

Flow apophyses act as attractors of material points, lines, and various other shapes in monoclinic flow types, but no stable fabrics can develop in markedly triclinic flows (Iacopini *et al.*, 2007); triclinic flow occurs when the vorticity vector is not parallel to one of the instantaneous stretching axes.

The kinematics of bulk flow in a shear zone must remain steady over the course of deformation in order for microstructural fabrics to preserve a meaningful record of W_k. Assumptions about the kinematics

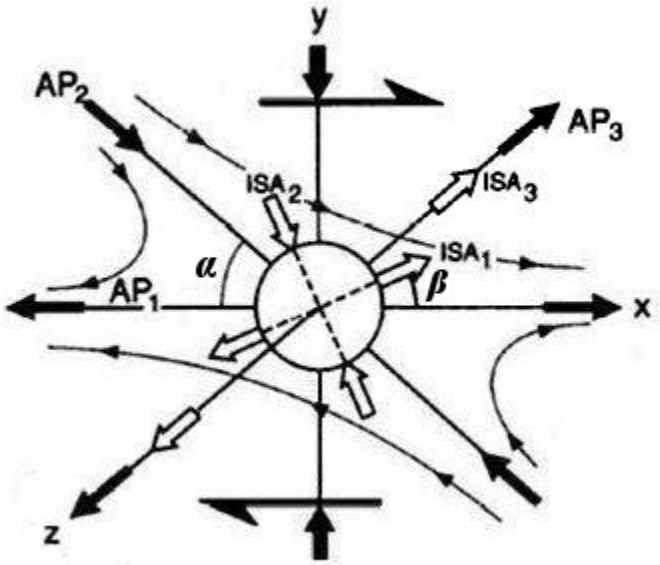

Figure 4: Diagram of monoclinic flow kinematics. All proceeding figures assume this frame of reference. ISA_1, ISA_2, and ISA_3 denote instantaneous stretching axes. AP_1, AP_2, and AP_3 denote velocity field eigenvectors ('finite strain axes' or 'flow apophyses'); AP_1 and AP_3 comprise the plane of zero instantaneous rotation ('flattening plane of finite strain' or 'flow plane'). For plane-strain (2-D) deformation, ISA_3 and AP_3 vanish because no material is flowing along the *z*-axis and the angle α defines the non-coaxiality of flow ($W_k = \cos(\alpha)$). Single-sided arrows indicate top-to-the-right sense of shear. Modified from Tikoff and Fossen (1995).

must take into account changes in boundary conditions over time (such as narrowing or widening of the shear zone, or changes in the tectonic plate convergence vector). Steady-state (constant $\dot{\varepsilon}$, $\dot{\gamma}$, and α) deformation is justifiable if boundary conditions are static. Kinematic processes driven by plate motion may be considered steady over sufficient time periods wherein plate convergence vectors do note change significantly over the course of deformation (Tikoff and Fossen, 1995).

If one can assume approximately steady-state, high strain, monoclinic, deformation in a mylonite zone, a number of methods can be applied to estimate the mean kinematic vorticity number W_m (W_k averaged over the course of deformation) in rock samples. For plane-strain flow, if β is the acute angle between the instantaneous stretching axes and flow apophyses (Fig. 4), then:

$$\beta = \frac{1}{2}(90° - \alpha) \tag{2}$$

$$W_m = \sin(2\beta) \tag{3}$$

At the final stage of deformation, new (dynamically recrystallized) quartz grains are stretched in the direction of ISA_1 (Fig. 5). Older quartz grains will have become stretched in the direction of AP_1 and undergone lattice reorientation along crystallographic planes or 'slip systems', assuming lattice preferred orientations (LPO) characterized by a type-II cross-girdle in 2-D projections of 3-D *c*-axis poles (Fig. 6). Type-II cross-girdles in natural examples (*e.g.*, Schmid and Casey, 1986; Wallis, 1995; Hubbard and Wang, 1999) are consistent with fabrics predicted by numerical experiments (*e.g.*, Lister and Hobbs, 1980; Wenk *et al.*, 1989; Jessell and Lister, 1990; Takeshita *et al.*, 1999) and observed in high *P-T* deformation experiments (*e.g.*, Tullis *et al.*, 1973; Tullis, 1977) in plane-strain conditions.

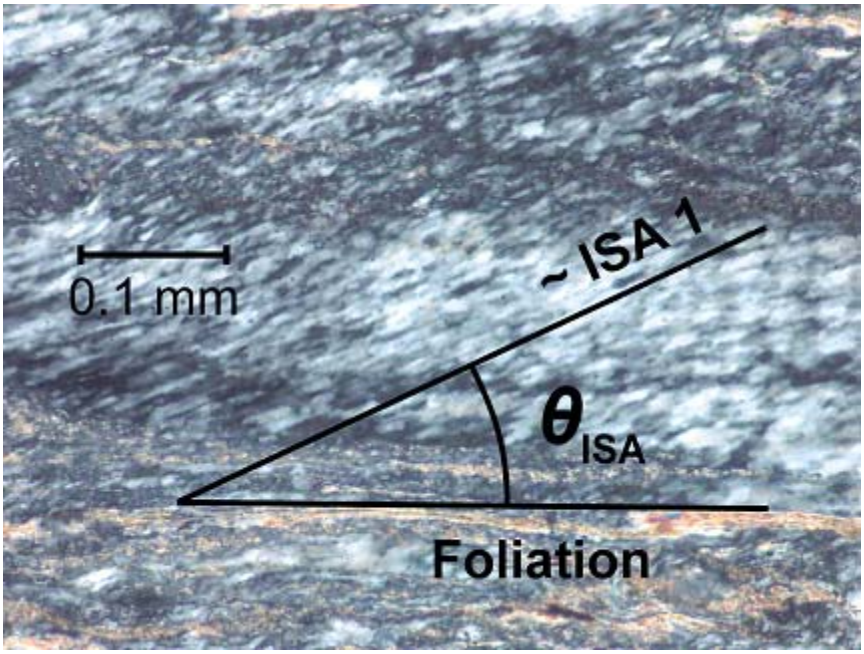

Figure 5: A 'snapshot' at the last increment of deformation: new quartz grains stretched in the direction of ISA_1. The maximum angle θ_{ISA} between the foliation and new grains contains information about W_m. Image courtesy of Scott Johnson.

The angle between AP_1 and ISA_1 is determinable from the geometry of well-developed quartz *c*-axis patterns (Wallis, 1995). If θ_{ISA} is the maximum angle between the foliation and ISA_1 (inferred from dynamically recrystallized quartz grains; Fig. 5) and δ is the angle between the foliation and the normal to the cross-girdle (Fig. 7), then:

$$\beta = \theta_{ISA} + \delta \quad (4)$$

$$W_m = \sin(2\theta_{ISA} + 2\delta) \quad (5)$$

Herein this 'dynamically recrystallized quartz method' of estimating W_m is referred to as Method 1.

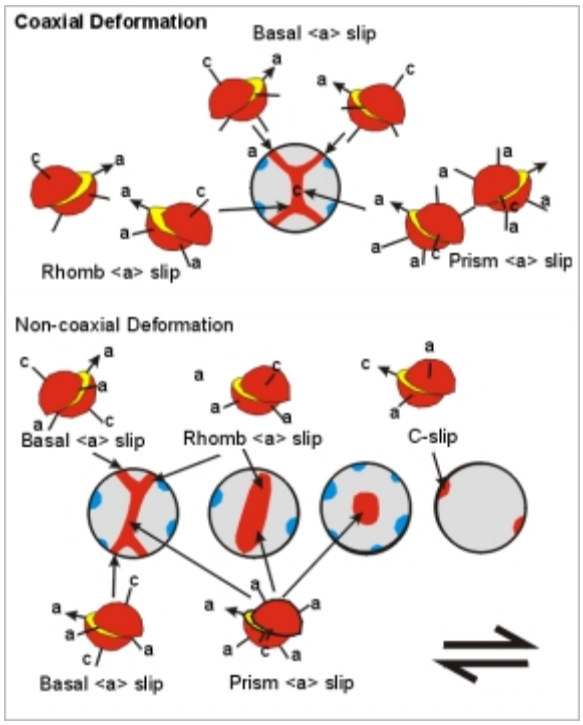

Figure 6: Diagram showing various 'slip systems' in which lattice reorientation occurs as quartz grains assume lattice-preferred orientations (LPO) with progressive deformation. Circular plots are 2-D projections of hypothetical 3-D quartz *c*-axis poles in lower hemispheres. Symmetric cross-girdles develop in coaxial (pure shear) flows whereas asymmetric and single girdles develop in general non-coaxial flows. Modified from Passchier and Trouw (2005); image courtesy of Scott Johnson.

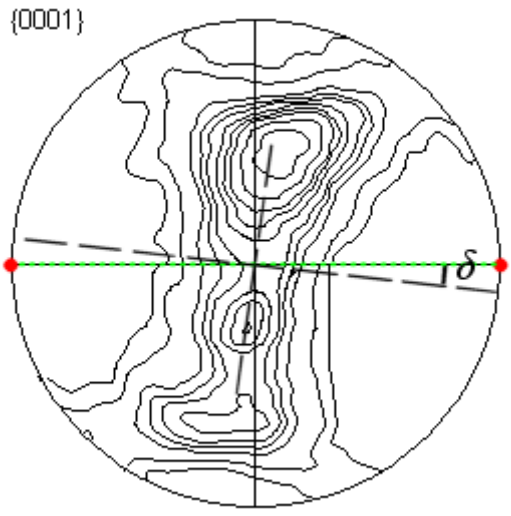

Figure 7: 2-D projections of 3-D quartz *c*-axis poles in a lower hemisphere. The lineation (red dots) lies in the plane of the foliation (green dotted line) oblique to the normal to the cross-girdle by a small angle δ. This angle contains information about W_m (Eq. 5) and becomes vanishingly small with progressive deformation. Sense of shear is top-to-the-right. Data and image courtesy of Nancy Price.

A different method of kinematic vorticity analysis exploits the rotational behavior of heterogeneities (herein interchangeably referred to as porphyroclasts, clasts, particles, and inclusions) in deformed rocks such as mylonites. Rocks exhumed from mylonite zones commonly contain porphyroclasts whose regular shape often resembles a parallelopiped, cylinder, or ellipsoid. The cross-sectional shape and orientation of a clast can be approximated as an ellipse with major and minor axes (m_i) (typically expressed as the cross-sectional shape factor $B^* = (m_1^2 - m_2^2)/(m_1^2 + m_2^2)$ after Bretherton, 1962, or aspect ratio $R^* = m_1/m_2$) and angle θ between the major axis and foliation plane (Fig. 8).

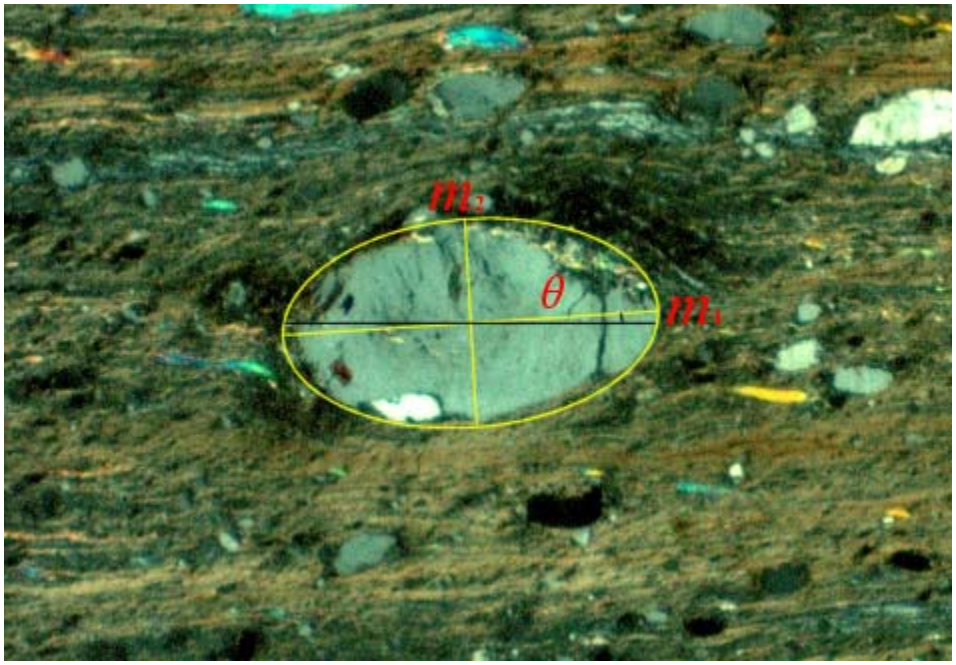

Figure 8: A best-fit ellipse (yellow) approximates the cross-sectional shape of a feldspar porphyroclast with major and minor axes (m_i), shape factor B^*, and orientation θ relative to the foliation (black horizontal line). Sense of shear is top-to-the-right.

The study of the motion of rigid particles in slow viscous flows followed Einstein's (1906) theory of Brownian motion in which he considered the motion of such particles suspended in low-viscosity fluids. Jeffery's (1922) theory predicts that uniaxial ellipsoidal rigid particles (with true shape factors B) in a viscous medium undergoing simple shear rotate synthetically (forward with respect to the sense of shear) as

a function of B, θ, and the shear strain rate $\dot{\gamma}$. Ghosh and Ramberg (1976) studied the rotational behavior of such particles in general non-coaxial flow ($0 < W_k < 1$) and derived an equation describing their motion:

$$\dot{\theta} = \frac{\dot{\gamma}}{2}[1 - B\cos(2\theta) - \frac{B}{W_k}\sqrt{1 - W_k^2}\sin(2\theta)] \quad (6)$$

$$= \frac{1}{R^2 + 1}[\dot{\gamma} R^2 \sin^2(\theta) + \dot{\gamma}\cos^2(\theta) - (R^2 - 1)\dot{\varepsilon}\sin(2\theta)] \quad (7)$$

Particles with shape factors above a critical value (B_{crit}) rotate toward and asymptotically approach a stable orientation θ_s whereas rounder particles rotate continuously in the flow. The stable orientation is sensitive to B and W_k:

$$\theta_s = -\frac{1}{2}\sin^{-1}\{\frac{W_k}{B}(\sqrt{1 - W_k^2} - \sqrt{B^2 - W_k^2})\} \quad (8)$$

$$= -\cot^{-1}\{s_r(R^2 - 1) + \sqrt{s_r^2(R^2 - 1)^2 - R^2}\} \quad (9)$$

Particle rotation also ceases at a second, metastable orientation θ_m for those particles more elongate than the critical shape factor:

$$\theta_m = \frac{1}{2}\sin^{-1}\{\frac{W_k}{B}(\sqrt{1 - W_k^2} - \sqrt{B^2 - W_k^2})\} - \frac{1}{2}\sin^{-1}(\sqrt{1 - W_k^2}) \quad (10)$$

$$= -\cot^{-1}\{s_r(R^2 - 1) - \sqrt{s_r^2(R^2 - 1)^2 - R^2}\} \quad (11)$$

The acute angle between the metastable and stable particle orientations ($\theta_m < \theta < \theta_s$) defines a field of antithetic (backward) rotation; the remaining range ($\theta_s < \theta < \theta_m$) defines a field of synthetic (forward) rotation. The metastable orientation is highly transient and, unlike the stable orientation, is not typically observed in analog experiments and natural examples.

The stable orientation enables a method for estimating the mean kinematic vorticity number W_m in mylonites and other high strain rocks that examines trends in the cross-sectional shapes (B^*) and orientations (θ) of porphyroclasts (*e.g.*, Passchier, 1987; Xypolias and Koukouvelas, 2001; Jessup *et al.*, 2007), albeit one that method commonly yields low estimates of W_m compared to other methods (*e.g.*, Wallis, 1995; Law *et al*., 2004).

In theory, there is a sharp transition between the shape preferred orientation (SPO) of clasts more elongate than the critical shape factor B^*_{crit} (strong clustering at $\theta = \theta_s$; see Eq. 7 and 8) and those continuously rotating (weak clustering at $\theta = 0$). The critical shape factor B^*_{crit} records W_m:

$$W_m = B^*_{crit} = \frac{R^{*2}_{crit} - 1}{R^{*2}_{crit} + 1} \tag{12}$$

Herein this 'rotated porphyroclast method' of estimating W_m is referred to as Method 2; a similar method developed by Simpson and De Paor (1993) characterizes the rotational behavior of clasts based on the geometry of their 'tails' (Fig. 3) but is not explored in this thesis.

The application of Methods 1 and 2 requires a geologic setting wherein the respective crystallographic and shape preferred orientation fabrics are well-developed and well-preserved. The following section of this thesis establishes a suitable observatory for conducting these kinematic vorticity analyses.

Geological setting and justifications for study

The Norumbega Fault System (NFS; Fig. 9) comprises the roots of a long-lived, Paleozoic, right-lateral, large-displacement, plate boundary-parallel, seismogenically active strike-slip fault system. Non-coaxial deformation features in south-central and south-coastal Maine are divided into two types: (1) a wide zone (>30 km) of heterogeneously spread structures consistent with right-lateral shear; (2) narrower zones (1–2 km wide) of high strain mylonites (West, 1999).

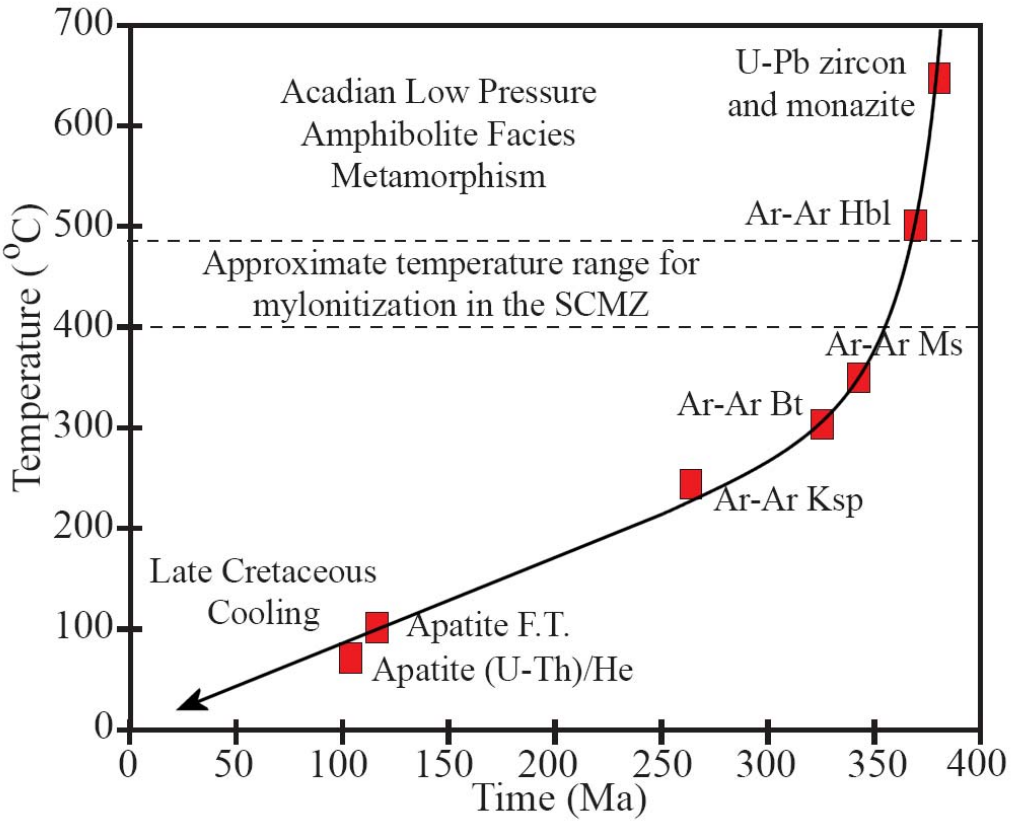

Figure 8: Thermochronological 'track' of rocks in the region of the SCMZ (black arrow) obtained from various radiometric dating methods. Data from West (1999), West and Lux (1993), West et al. (1988; 1995; 2006), Tucker *et al.* (2001), and Gerbi and West (in review); image courtesy of Scott Johnson.

Among these strands of localized deformation in the NFS is the Sandhill Corner Mylonite Zone (SCMZ; Fig. 7), a 100 to 300 m wide zone of mutually overprinting mylonite and pseudotachylyte. An absolute age of mylonitization in the SCMZ has been established (West and Lux, 1993), placing the mutually overprinting mylonite and pseudotachylyte into the regional time-temperature chronology (Fig. 8).

The following observations suggest the SCMZ is an ideal place for conducting kinematic vorticity analyses (the relevance of these observations is expounded in more detail below): (1) Equal area projections of foliations and lineations in the SCMZ and other mylonite zones in south-central Maine reveal a subvertical foliation and subhorizontal lineation consistent with the regional trend. (2) Sections perpendicular to foliation and parallel to lineation exhibit strong fabric asymmetry. In contrast, fabrics in the two mutually orthogonal sections are markedly symmetric. (3) Quartz c-axis pole figures (Fig. 7; see Fig. 5 in Hubbard and Wang, 1999) exhibit type-II cross-girdle patterns with maxima in the plane of foliation and perpendicular to lineation.

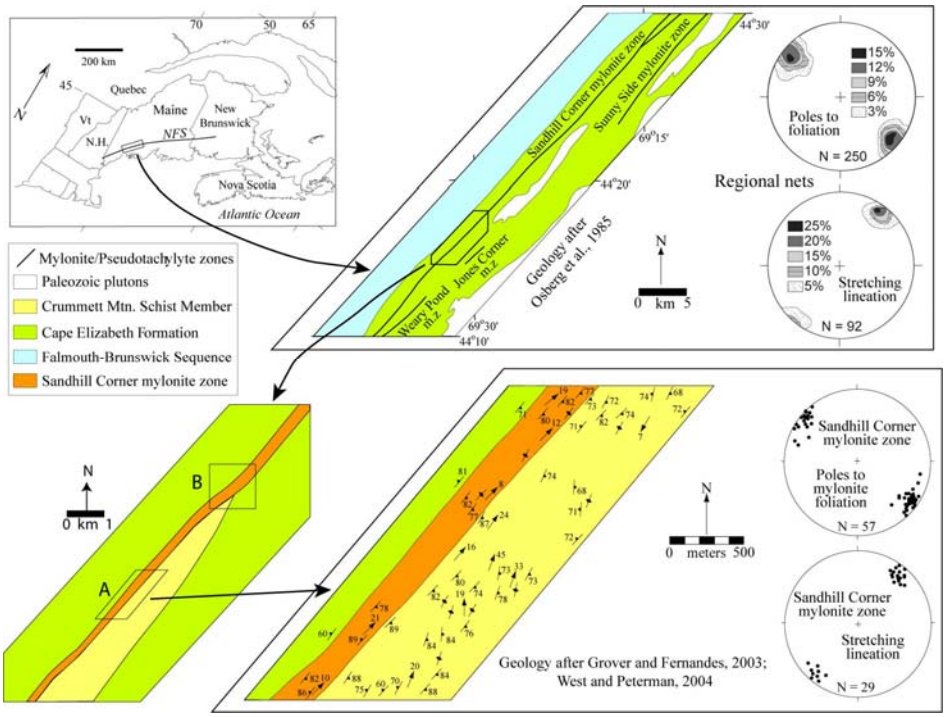

Fig. 9: Geological maps of the field area and surrounding region. Circular plots are 2-D projections of 3-D linear data in a lower hemisphere. Image courtesy of Scott Johnson.

Field work and sample preparation

Samples of SCMZ mylonites were collected in a field area approximately 200 m × 200 m and adjacent to the contact between the mylonites and the Crummett Mountain Schist member. The orientations of samples were recorded using a geological compass. Samples were taken to the University of Maine Dept. of Earth Sciences and cut into 1" × 2" sections parallel to lineation and perpendicular to foliation. In preparation for microscope analysis, samples were polished and mounted onto glass slides using epoxy, cut off leaving ~2 mm on glass, progressively ground down to a thickness of ~20 μm, and fitted with glass cover slips. (The final thickness of thin sections facilitates the transmission of light for optical analysis.)

Kinematic vorticity analyses

1. *Assumptions*

The key assumptions required for employing microstructural methods to estimate W_m in SCMZ mylonites are:

(1) Shearing in the vertical direction was negligible compared to shearing in the horizontal plane. Non-negligible vertical velocity gradients from the edges to core of the SCMZ would imply a significant component of vorticity in the foliation plane as well as in the horizontal plane (defining a markedly triclinic flow). This component is not measurable in thin sections parallel to lineation and perpendicular to foliation, but is assumed to be insignificant.

(2) Deformation was near steady-state at the time microstructures were 'frozen in'. The components of the velocity gradient tensor (see Appendix 1) would be changing with time if deformation were not steady-state. Abrupt changes in kinematics would prevent time-averaged W_m measurements made using Method 2 from reflecting the time-dependence of W_k (Method 1 has similar limitations, measuring W_m at the last increment of deformation). W_k is assumed to have remained approximately constant over the course of deformation so that W_m estimates give a meaningful time-average.

(3) Post-exhumation deformational and thermal overprint is minor. Overprinting would reduce fabric intensities or make them reflect a later phase of deformation, so it is assumed that microstructures in the SCMZ preserve W_m during mylonitization. Thermochronological studies provide no evidence of post-mylonitic deformation in the region surrounding the SCMZ (West and Lux, 1993).

2. *Method 1: Dynamically recrystallized quartz*

Two measurements are necessary to determine β in a given sample: the angle θ_{ISA} between the foliation and the direction of elongation of new quartz grains (Fig. 5), and the angle δ between the foliation and the normal to the quartz *c*-axis girdle (Fig. 7). The former is measured in SCMZ samples using a *Nikon*

"Eclipse E600 POL" microscope and the latter is measured using a *LEO* "1450 VP" scanning electron microscope with electron backscatter diffraction (Lenferink *et al.*, in preparation).

Because the foliation is not perfectly planar at the thin section scale, estimates of W_m using Method 2 require several measurements of θ_{ISA} in each sample; the mean value and standard deviation of these measurements provide a range of W_m estimates.

3. *Method 2: Rotated porphyroclasts*

Passchier (1987) introduced five basic criteria for the analysis of clast SPO: (1) the sample accumulated high finite strain so that a fabric could develop; (2) the fabric indicates homogeneous deformation on the scale of the sample; (3) the matrix grain size is much smaller than that of clasts; (4) clasts have regular shape and may be approximated by orthorhombic (or ellipsoidal) symmetry; (5) the shape factor of clasts is well-dispersed. SCMZ samples meet these core requirements, but it is difficult to differentiate between clasts that had assumed stable orientations and those that rotated continuously in the flow. Therefore a large number of measurements (>200) is required to reveal trends in the fabric.

For each sample, sets of photomicrographs were taken using a *Diagnostic Instruments* "SPOT RT Color" camera and a *WILD* "M420" macroscope. The best-fit ellipse algorithm in the photo editing software *ImageJ* assigned a major and minor axis (m_i), cross-sectional shape factor (B^*) and orientation (θ) to individually-selected feldspar porphyroclasts (Fig. 8). Following Ghosh and Ramberg's (1976) theory of particle rotation and Passchier's (1987) criteria, W_m is determined from the shape factor 'cut-off' between clasts that had apparently reached a stable orientation (high B^*) and those that apparently rotated continuously (low B^*).

4. *Results*

Tab. 1 displays ranges of W_m estimates made using Methods 1 and 2. Fig. 10–14 plot the cross-sectional shapes and orientations of porphyroclasts for each sample. In all samples the distribution of round clasts ($0 < B^* < 0.4$) is scattered but symmetric about the foliation, weakly clustering at $\theta = 0$. The

distribution of clasts with intermediate shapes ($0.4 < B^* < 0.6$) is asymmetric about the foliation, strongly clustering at small negative angles. The distribution of elongate clasts ($0.6 < B^* < 1$) is asymmetric about the foliation, strongly clustering at small positive angles. In all samples the cut-off between strong and weak clustering of clast orientations is not distinct but occurs over a range of B^* values (~0.1).

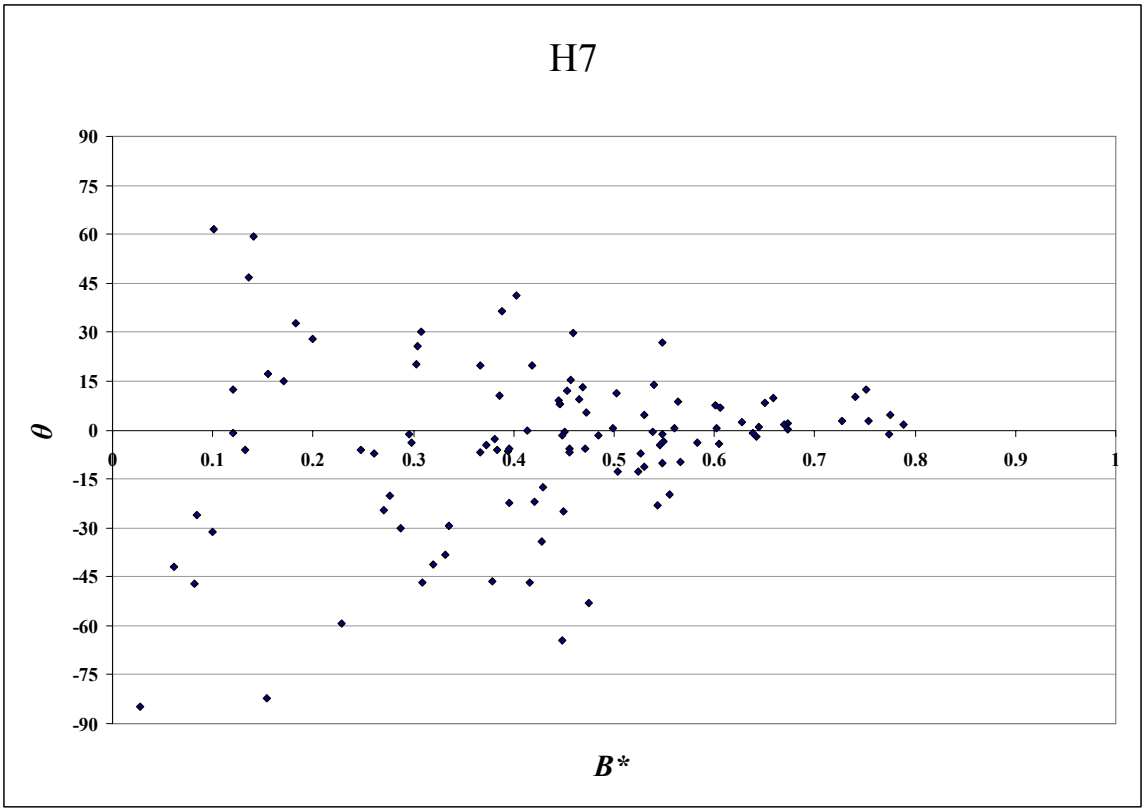

Figure 10: Clast data for sample H7 (107 data points).

Figure 11: Clast data for sample H8 (270 data points).

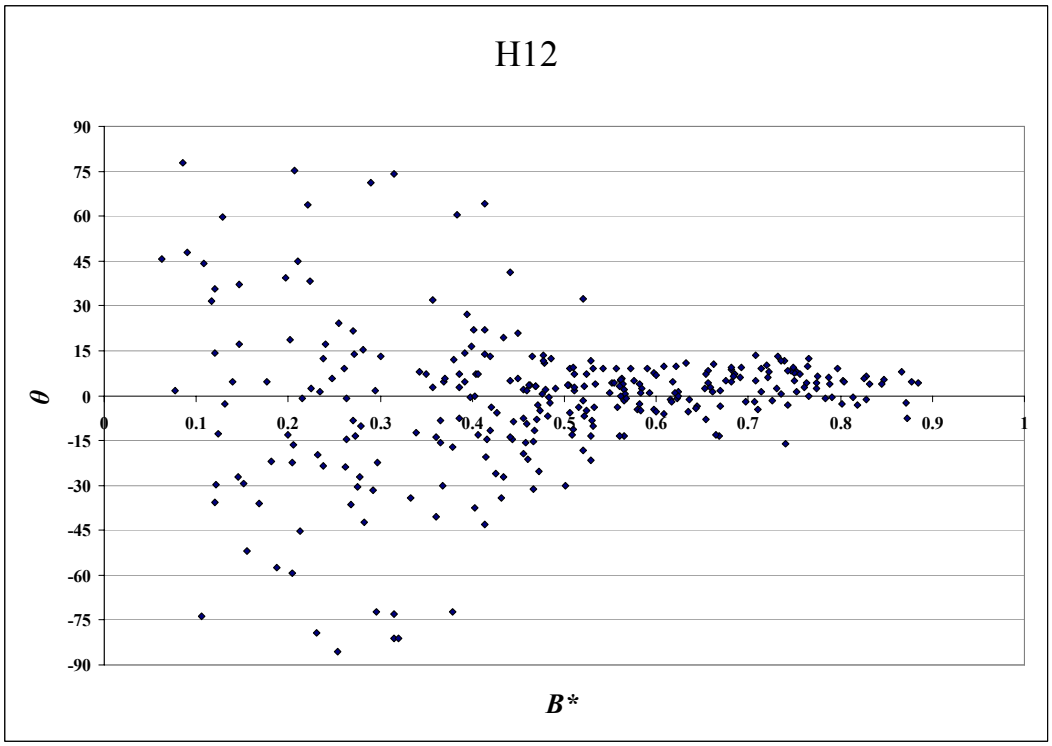

Figure 12: Clast data for sample H12 (300 data points).

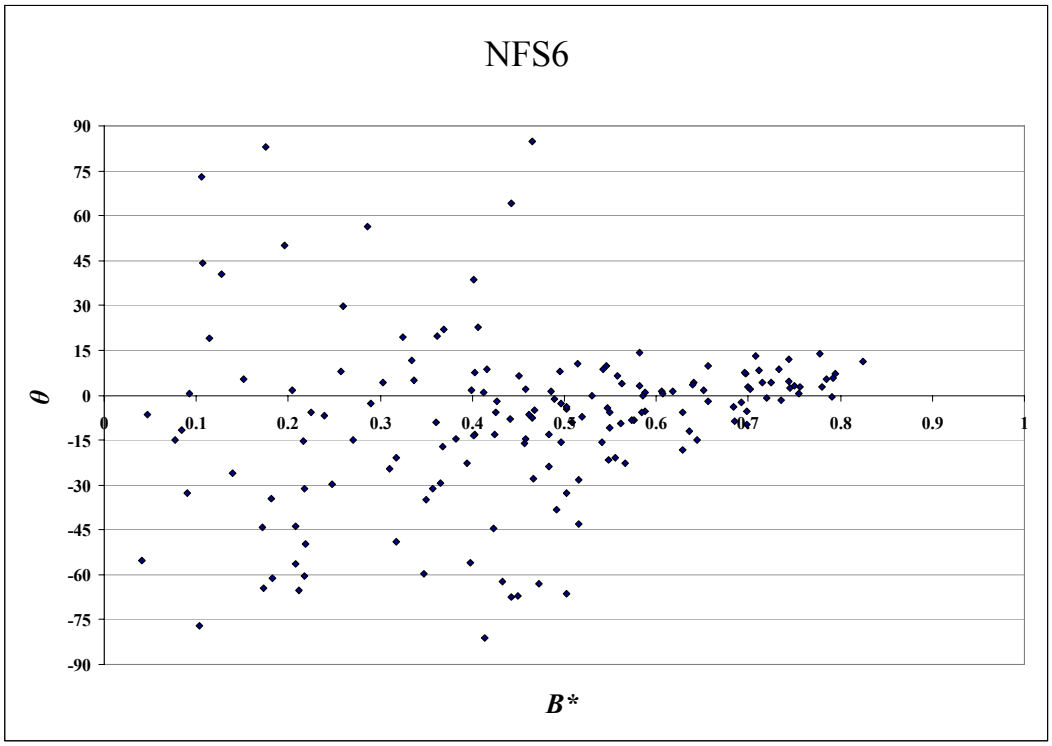

Figure 13: Clast data for sample NFS6 (160 data points).

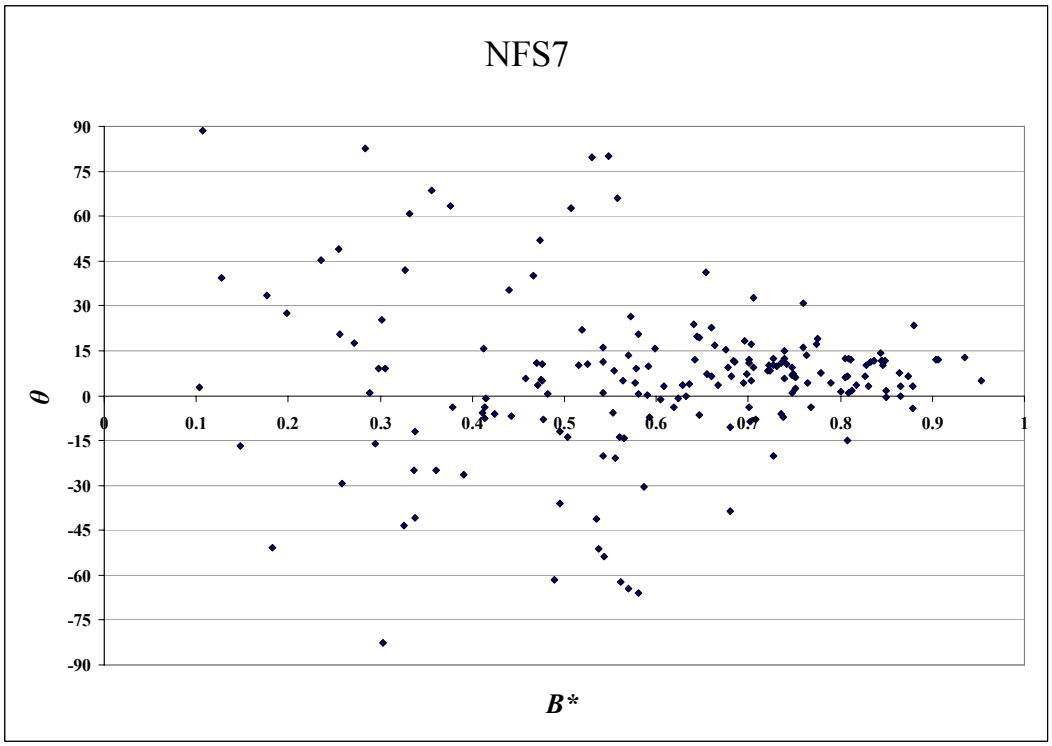

Figure 14: Clast data for sample NFS7 (186 data points).

Sample	W_m (*Method 1*)	W_m (*Method 2*)
H7	0.90 – 0.97	0.4 – 0.5
H8	0.95 – 0.98	0.3 – 0.4
H12	0.97 – 1.00	0.4 – 0.5
NFS6	0.94 – 1.00	0.4 – 0.5
NFS7	0.94 – 0.99	0.5 – 0.6

Table 1: Ranges of mean kinematic vorticity number W_m obtained using Methods 1 and 2.

5. *Discussion*

Estimated W_m values range from 0.3 to 1 depending on the sample, method applied, and uncertainties associated with each method. Though both methods indicate significant components of simple shear in all samples, W_m values obtained via Method 2 are consistently lower than those obtained via Method 1 within individual samples.

A number of explanations for this discrepancy are plausible: (1) requirements of the individual methods are not satisfied (*e.g.*, Method 2 underestimates W_m if few elongate clasts are present in the sample, in which case the upper bound of the W_m range is most accurate; see Law *et al.*, 2004); (2) the two methods record different episodes of the strain history (*e.g.*, Method 1 can only access the last instant of deformation, having a shorter 'strain memory' than Method 2); (3) assumptions regarding the validity of one or both of the methods are incorrect.

The first explanation does not likely hold; the upper bound of W_m measured using Method 2 is much lower than the lower bound of W_m using Method 1 even for data sets containing a few hundred clast measurements (Fig. 11 and 12). The second explanation is conceivable, but suggests that deformation was not near steady-state (*i.e.*, that the angle α between the flow apophyses was changing with time). The third invites the following two considerations:

(1) The interaction of porphyroclasts affects their rotational behavior and surrounding flow patterns (Ildefonse and Mancktelow, 1992; Samanta *et al.*, 2003). A major precondition for using Method 2 to estimate W_m is that clasts rotated as solitary, isolated objects in the rock matrix (Ghosh and Ramberg's (1976) theory does not incorporate clast interaction). According to Ghosh and Ramberg's (1976) theory,

SPO fabric strength should grow with progressive deformation for a given clast population and be independent of shape factor after large finite strain. However, synkinematic fracturing and fragmentation of parent clasts produces new, angular clasts which separate away and begin to rotate in the flow. The interaction of clasts is most significant in those areas where new ones were being created when deformation ended. A criterion of selecting isolated, whole, rounded clasts for analysis helps ensure they had the chance to reach stable orientations, thus minimizing the effects of clast interaction on SPO fabric strength.

(2) A second precondition for using Method 2 to estimate W_m is that perfect viscous coupling occurred between clasts and the rock matrix. The rotational behavior of 'tailed' porphyroclasts (Fig. 3), also called 'porphyroclast systems' (Passchier and Simpson, 1986), is strongly influenced by strain localization around clasts, compromising the reliability of clast SPO as an indicator of W_m. Various analog experiments (Ildefonse and Mancktelow, 1993; Passchier and Sokoutis, 1993; ten Brink and Passchier, 1995; Mancktelow *et al*., 2002; ten Gruitenhuis *et al*., 2002; Marques and Bose, 2004) and recent numerical modeling experiments (Marques *et al*., 2005; Schmid and Podladchikov, 2005; Johnson, 2008) have shown that strain localization arising from a thin low-viscosity layer (LVL; dark shaded region in Fig. 17) or other slip condition at the surfaces of rigid particles in slow viscous flows can markedly affect the rotational behavior of those particles.

In a series of numerical modeling experiments, the following section of this thesis explores the relaxation the second precondition. The purpose of this endeavor is to see how the rotational behavior of clasts changes when lubrication occurs at their margins and whether such changes could effect a discrepancy between Methods 1 and 2.

Numerical modeling of porphyroclast systems

1. *Model description*

COMSOL Multiphysics employs the finite element method (FEM), a computational method that discretizes an object into several polygonal elements (triangles in Fig. 15) which form a mesh. The program assigns each element a set of characteristic equations describing the physical properties, imposed forces, and boundary conditions of the element; these equations are then solved simultaneously for all elements to predict the behavior of the object (COMSOL AB, 2006).

The fluid-structure interaction capability of the *COMSOL Multiphysics* "Structural Mechanics" module serves as a basis for studying the SPO of an isolated, rigid ellipsoidal particle suspended in a steady monoclinic flow. Because the fluid under investigation is incompressible and inertial terms are considered negligible, the Navier-Stokes equations reduce to

$$\nabla p = \eta \, \nabla^2 \boldsymbol{v} \qquad\qquad \nabla \cdot \boldsymbol{v} = 0$$

The boundary conditions of a 2-D 'shear box' (Fig. 16) define the flow type, with end members ranging from pure shear ($W_k = 0$) to simple shear ($W_k = 1$). An elliptical particle is located at the center of the shear box; its shape B, initial orientation θ_i, and the ratio of viscosities $\tilde{\eta}$ between the low viscosity layer (LVL) enveloping the particle and the surrounding fluid medium are specified in each experiment.

In all experiments the viscosity η_{med} of the fluid medium is fixed at 10^{18} Pa s, the strain rate at 10^{-10} s^{-1}, the Young's modulus of the particle at $2 \cdot 10^{14}$ Pa, and the ratio of the LVL thickness to the particle radius at 5%. Also, the minor axis of the particle is fixed 10% the shear box width so as to minimize the effects of confined flow on particle rotation (see Fig. 5 in Marques *et al*., 2005).

As the fluid medium begins deforming, a torque imbalance may act on the particle (depending on θ_i):

$$\boldsymbol{N} = \boldsymbol{N}_\sigma + \boldsymbol{N}_\tau \qquad \boldsymbol{N}_\sigma = \oint_S \boldsymbol{r} \times \boldsymbol{n}\ \sigma\ da \qquad \boldsymbol{N}_\tau = \oint_S \boldsymbol{r} \times \boldsymbol{t}\ \tau\ da$$

Here $\boldsymbol{r}(x_S, y_S)$ describes the position of an area element of the surface of the particle, $\boldsymbol{n}(x_S, y_S)$ and $\boldsymbol{t}(x_S, y_S)$ are the normal and tangent unit vectors, respectively, and $\sigma(x_S, y_S)$ and $\tau(x_S, y_S)$ are the corresponding normal pressure and shear stress acting on the surface element da.

If a stable orientation θ_s exists for a given W_k, B, and $\tilde{\eta}$ (in other words, if $B > B_{crit}$) the net torque on the particle vanishes as the particle rotates toward and asymptotically approaches the stable orientation; if $B < B_{crit}$ the particle rotates continuously in the flow. In the former case, particle rotation is antithetic (forward) for $\theta_m < \theta < \theta_s$ and synthetic (backward) for $\theta_s < \theta < \theta_m$. Therefore it is possible to estimate θ_s for a given W_k, B, and $\tilde{\eta}$ based on the initial orientations of two models that differ slightly in θ_i (±0.25º) and exhibit opposite senses of rotation (the average of the two θ_i values approximates θ_s). Sensitivity analyses in W_k-B-$\tilde{\eta}$ parameter space are performed by this means, and the following results demonstrate how θ_s varies as a function of those parameters.

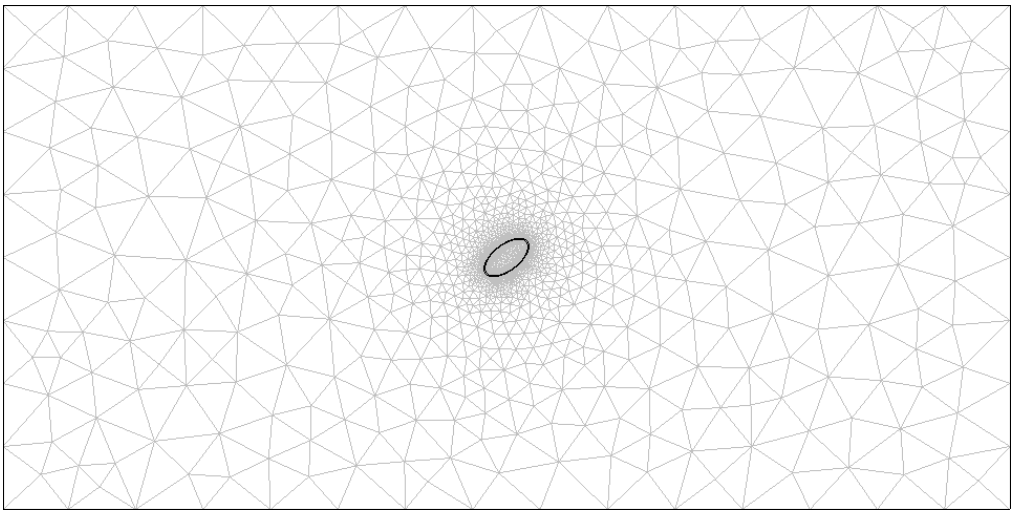

Figure 15: Mesh elements are finest in the vicinity of the particle system.

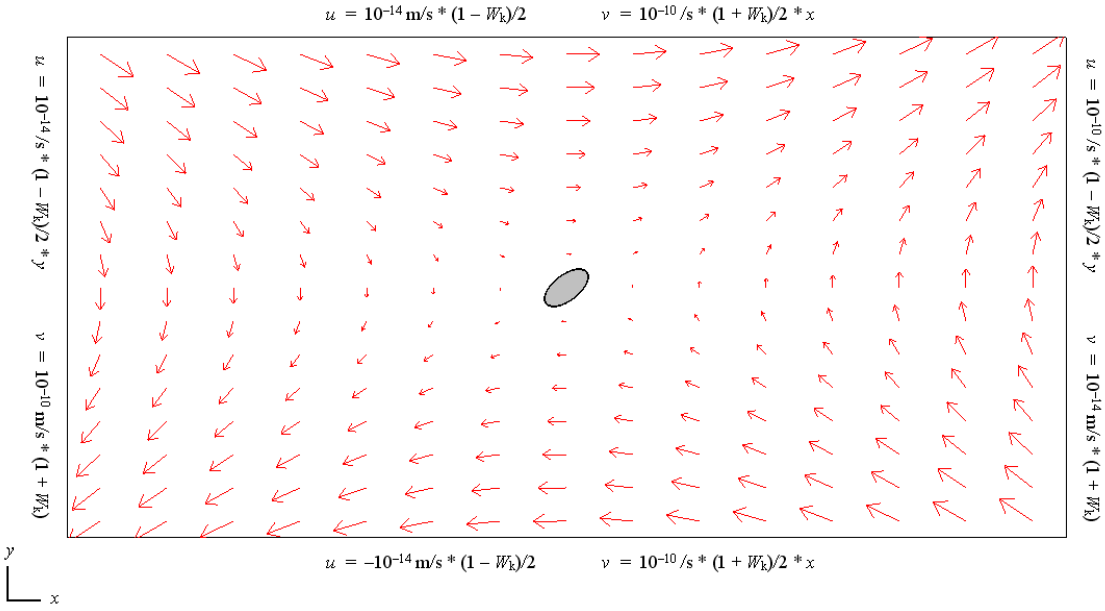

Figure 16: The 'shear box' has length $l = 2 \cdot 10^{-4}$ m and width $w = 10^{-4}$ m. The center of the particle system is located at (0, 0). Boundary conditions of the shear box are as given in terms of W_k. Along a given boundary, u specifies the component of velocity in the x-direction and v specifies the component of velocity in the y-direction. Red arrows indicate the magnitude and direction of velocity at various points inside the shear box. Sense of shear is top-to-the-right.

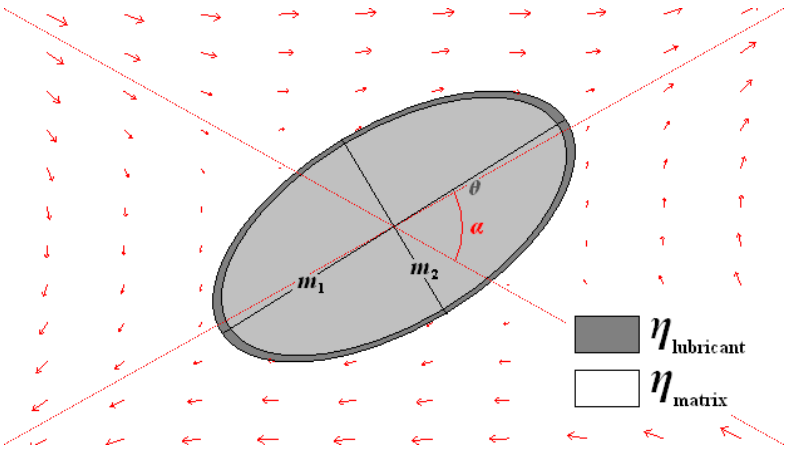

Figure 17: Close-up view of the particle system. Red arrows indicate velocity at points relative to the center of the particle. Dotted red lines denote the [far-field] flow apophyses. The particle (light shaded region) is effectively rigid compared to the surrounding fluid matrix. The thickness of the low viscosity layer (LVL; dark shaded region) enveloping the particle is 5% the radius of the particle.

2. *Results*

Fig. 19–22 each contain a 'family' of SPO curves representing the stable orientations θ_s of particles as a function of B for various W_k values (colored lines in Fig. 18–21) and a fixed viscosity contrast $\tilde{\eta}$. Perfectly coupled particles ($\tilde{\eta} = 1$; Fig. 19) exhibit SPO curves that are reclined ($\theta_s < 0$) with respect to AP_1 for all B, in agreement with Ghosh and Ramberg's (1976) solution.

Imperfectly coupled particles ($0 < \tilde{\eta} < 1$), on the other hand, exhibit SPO curves consisting of both reclined portions ($\theta_s < 0$) and inclined portions ($\theta_s > 0$). The reclined portion of each SPO curve terminates at a characteristic point on the 'B_{crit} envelope' of its family (dotted lines in Fig. 18–21). The inclined portions increase in amplitude with W_k and resemble parabolae for a considerable range of viscosity contrasts ($0.5 < \tilde{\eta} < 1$);

The lineation-parallel shape (LPS) transect (Fig. 22) reveals a characteristic shape B' that stably aligns parallel to AP_1 for a given $\tilde{\eta}$. All curves in a given family pass through the point (B', 0) so B' is independent of W_k. The relationship between B' and $\tilde{\eta}$ is approximately linear ($B' \approx 8\,\tilde{\eta}$) over a large range of shape factors ($0 < B' < 0.9$); B' is most sensitive to $\tilde{\eta}$ near unity ($0.9 < B' < 1$).

The SPO of clasts in simple shear ($W_k = 1$) can be represented as a function of B for various $\tilde{\eta}$ values (black curves in Fig. 21; corresponding $\tilde{\eta}$ values are given by B' in the LPS transect). As $\tilde{\eta}$ approaches zero, these curves approach the 'total slip envelope' (dashed line in Fig. 22; approximated by $\tilde{\eta} = 10^{-6}$). Presumably, like the inclined portions of SPO curves in Fig. 18–22, the total slip envelope varies in amplitude with W_k.

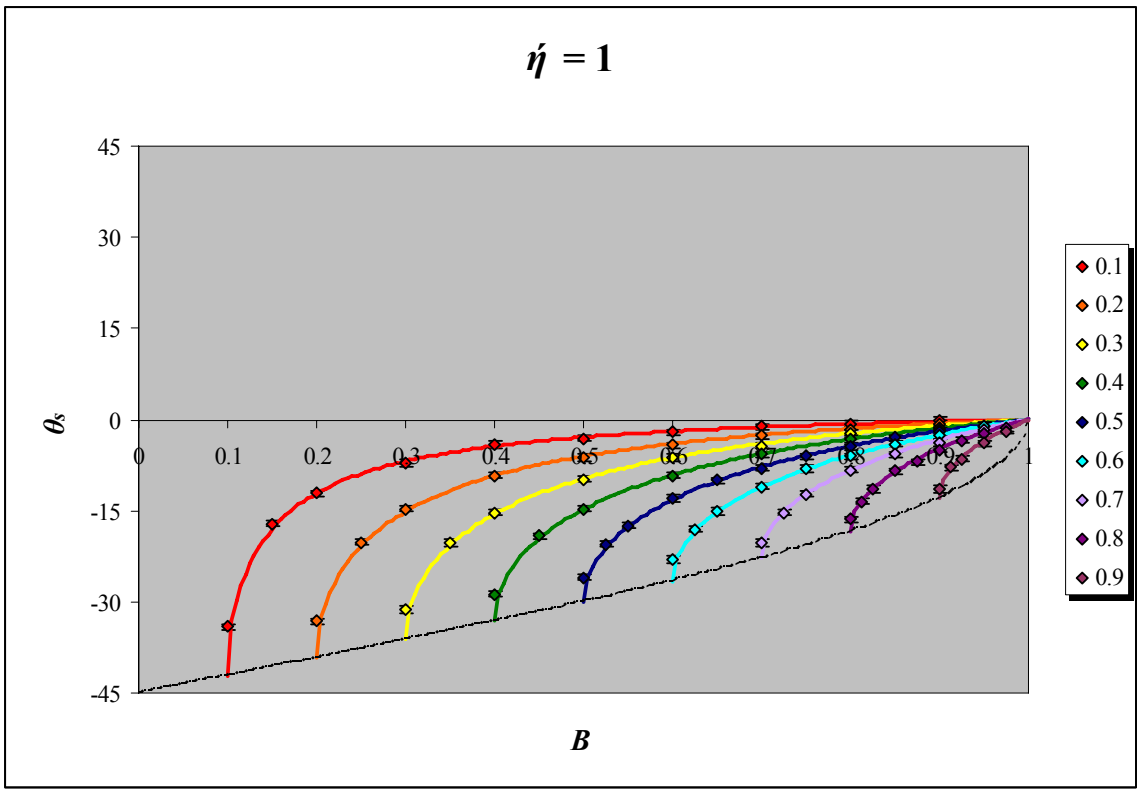

Figure 18: Colored lines are connect-the-dot curves of SPO trends. Each color corresponds to a specific W_k as indicated in the legend.

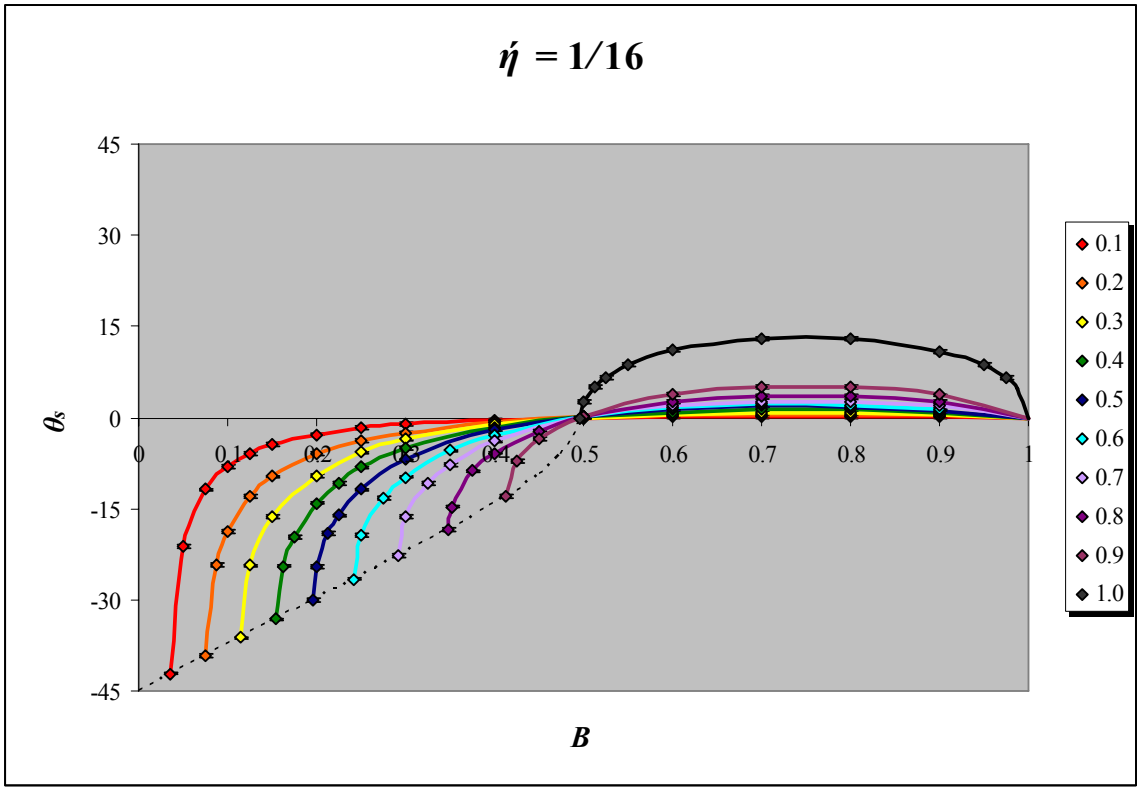

Figure 19: (see caption for Fig. 18)

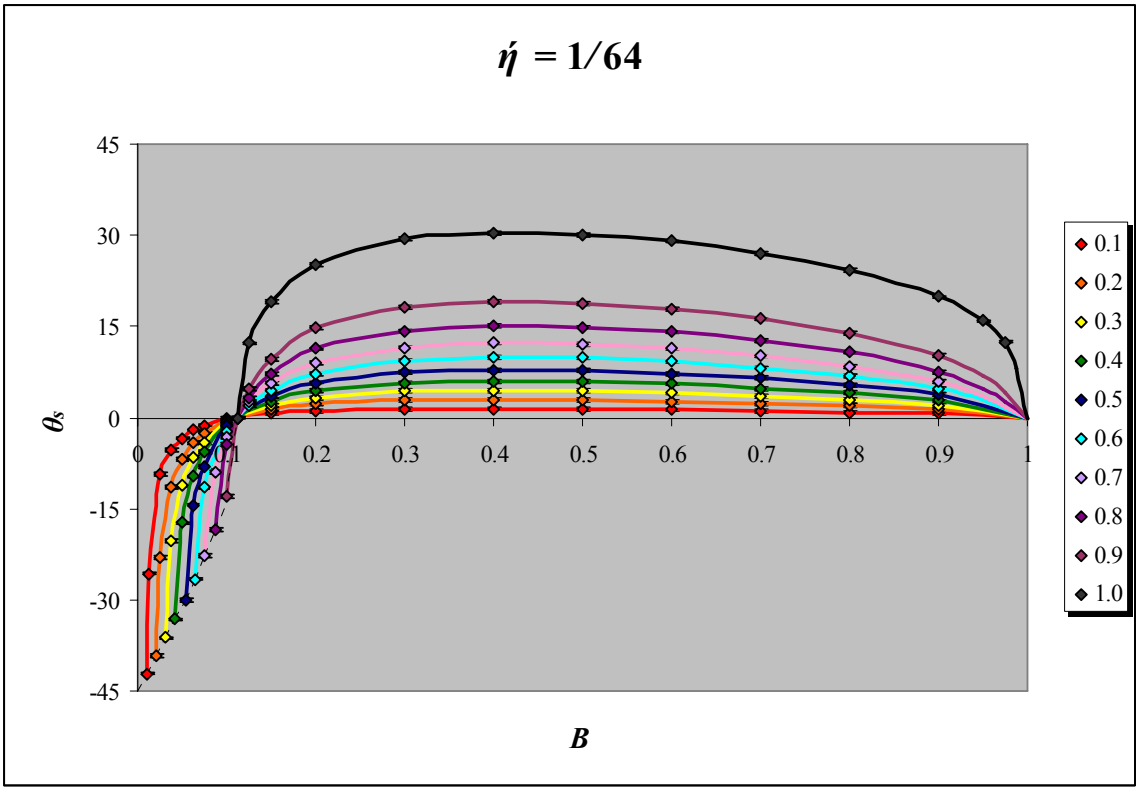

Figure 20: (see caption for Fig. 18)

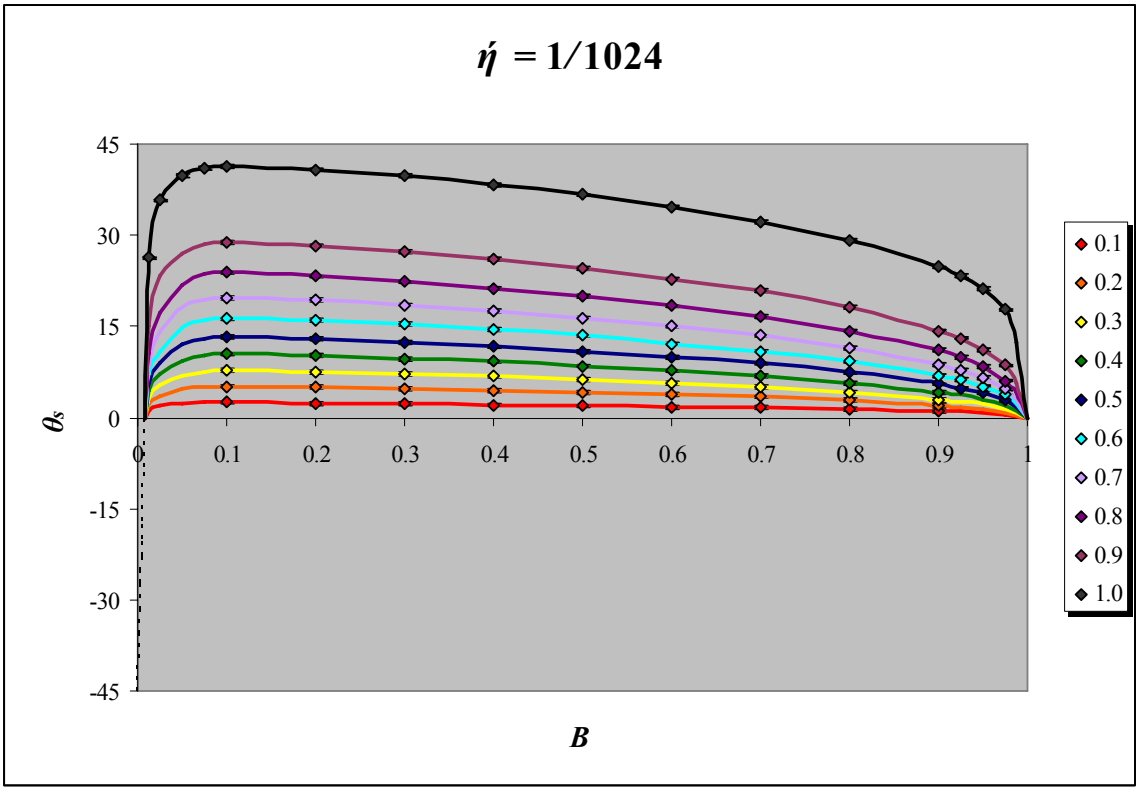

Figure 21: (see caption for Fig. 18)

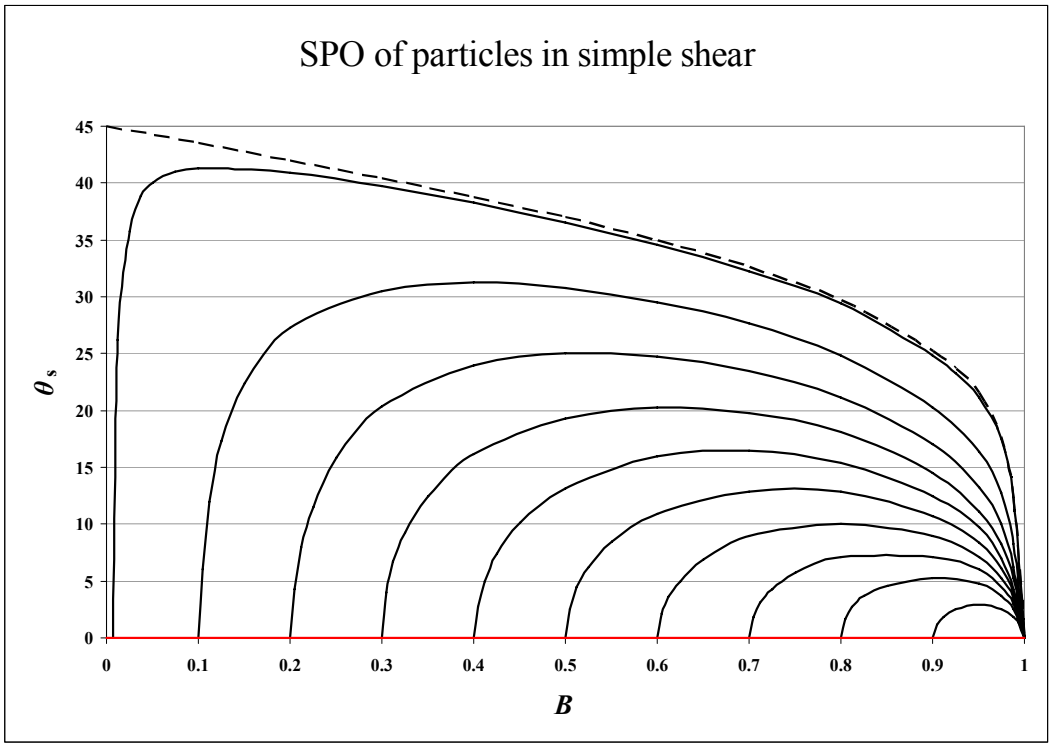

Figure 22: Black curves correspond to various $\widetilde{\eta}$ values indicated by B' in the LPS transect.

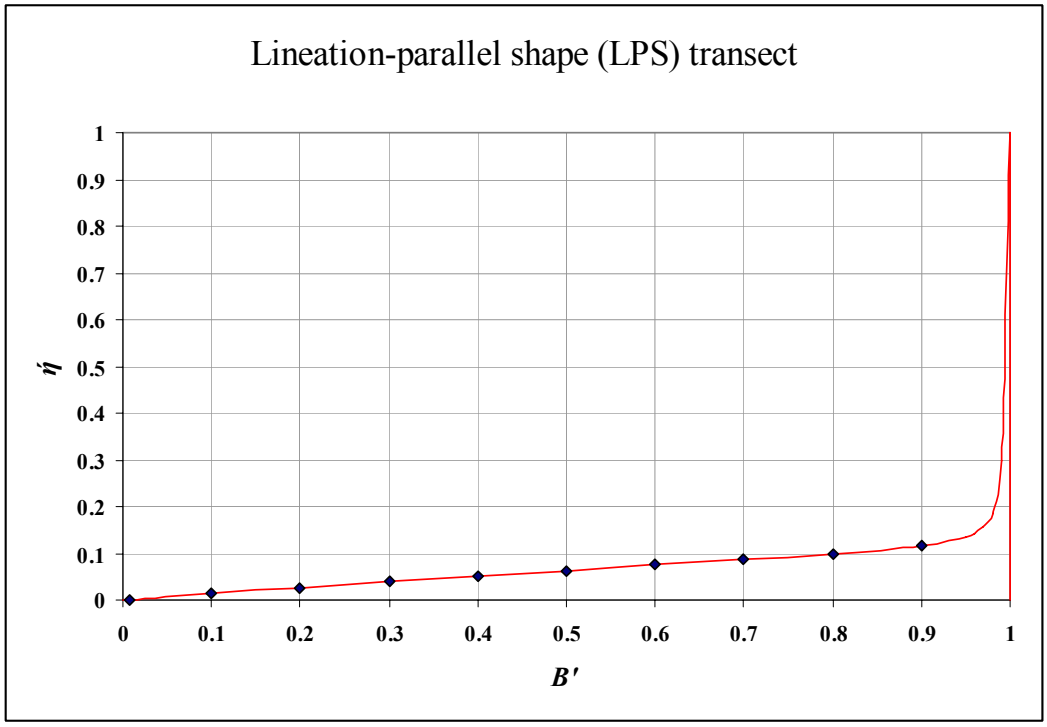

Figure 23: The lineation-parallel shape transect indicates the characteristic shape B' that aligns parallel to AP_1

3. *Discussion*

For lubricated particles ($0 < \tilde{\eta} < 1$) the shape factor cut-off B_{crit}, normally used to infer W_m in kinematic vorticity analyses, is lower than that predicted by Ghosh and Ramberg's theory. If $\tilde{\eta}$ is near unity (perfect viscous coupling), the SPO family resembles Ghosh and Ramberg's (1976) solution. But for the range $0 < \tilde{\eta} < 1$, the B_{crit} envelope is contracted to the left by greater or lesser amounts. As $\tilde{\eta}$ approaches zero, the reclined portions of the SPO curves vanish and the inclined portions approach a total slip envelope (represented by dashed line in Fig. 22 for $W_k = 1$; amplitude varies with W_k).

B_{crit} will always indicate low W_m if porphyroclasts are lubricated (or otherwise slipping) at their margins. However, the linearity of the LPS transect over the range $0 < B' < 0.9$ (Fig. 23) could enable estimation of $\tilde{\eta}$ of porphyroclasts. In this respect, $\tilde{\eta}$ is a paleo-viscosity contrast 'frozen' into the mylonite as deformation ended. Even if no strong SPO fabric is present (for example, if $\tilde{\eta}$ differs from one clast to another, leading to a spread of B'-intercepts) it should be possible at least to determine whether $\tilde{\eta}$ on average is close to zero, close to one, or an intermediate value. Such qualification alone could provide new insight into deformational processes at the microstructural scale in mylonites.

For the sake of demonstrating how one could estimate $\tilde{\eta}$ (assuming $W_m \approx 1$) from porphyroclast shapes and orientations with the aid of graphical tools, clast data presented in the previous section (Fig. 10–14) are re-plotted below (Fig. 24–28). Fig. 27 reveals a strong trend with a B'-intercept suggesting $\tilde{\eta}$ could range from 0.06 to 0.07 in sample H12 (according to the LPS transect; Fig. 23).

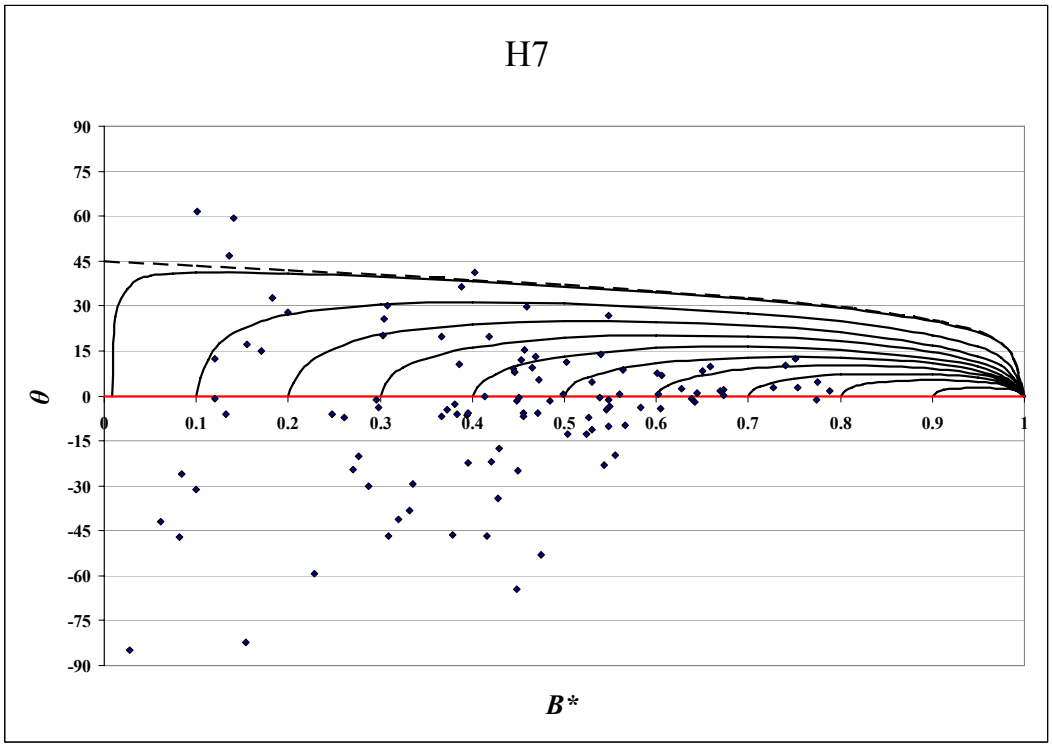

Figure 25: (see caption for Fig. 10)

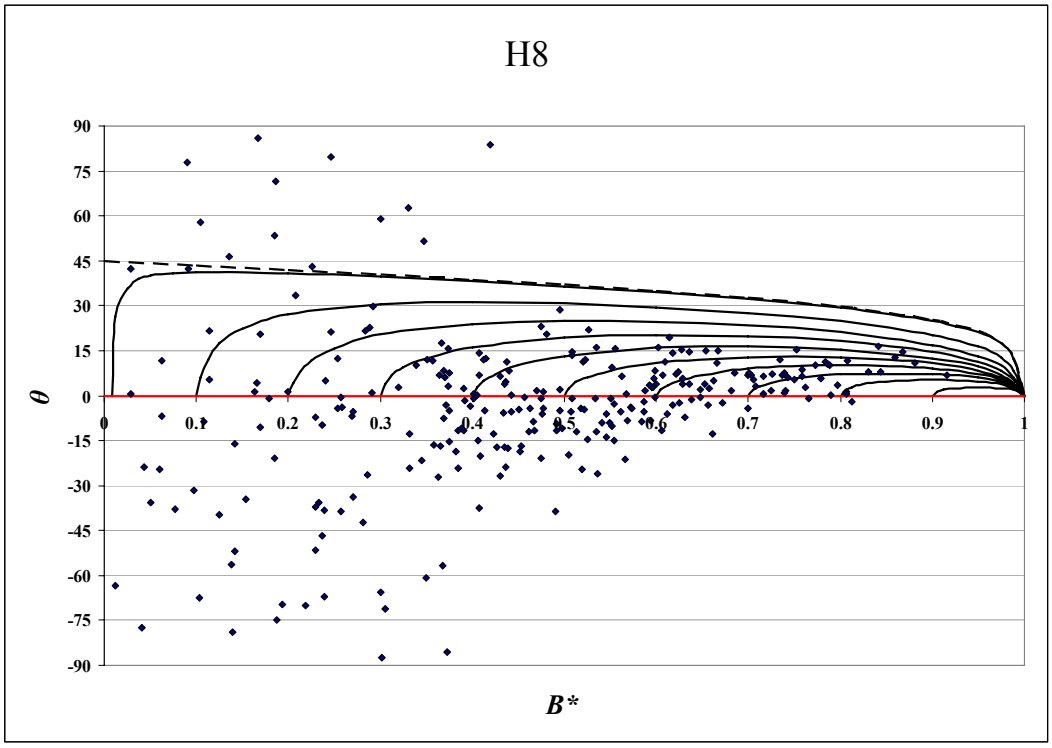

Figure 26: (see caption for Fig. 10)

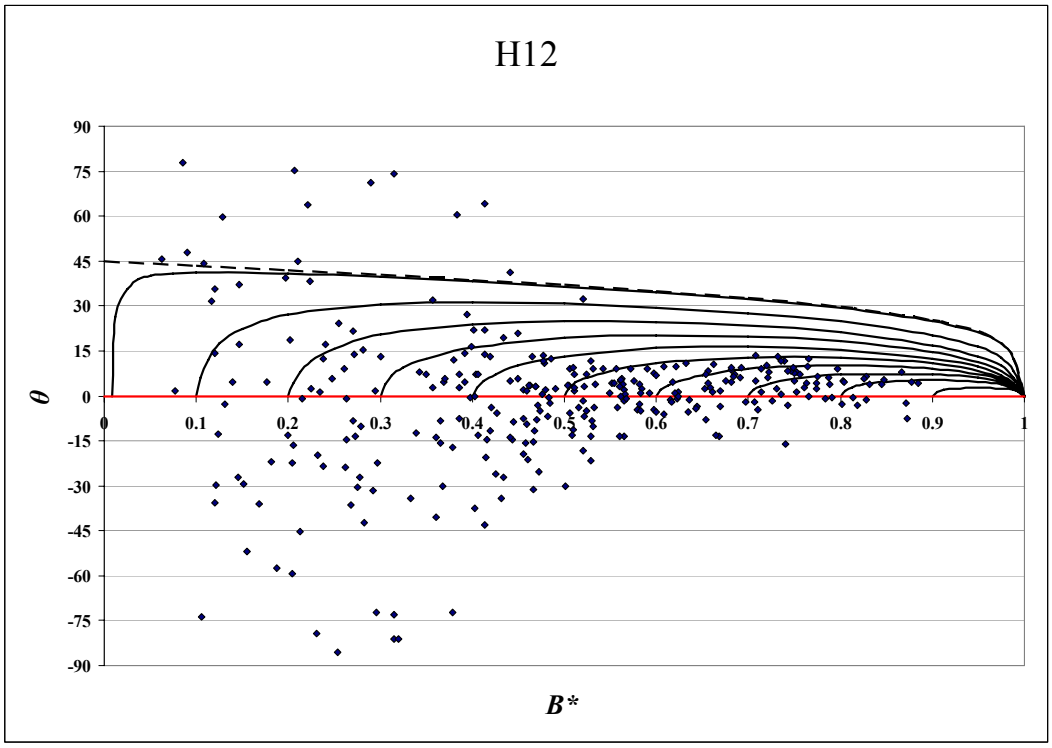

Figure 27: (see caption for Fig. 10)

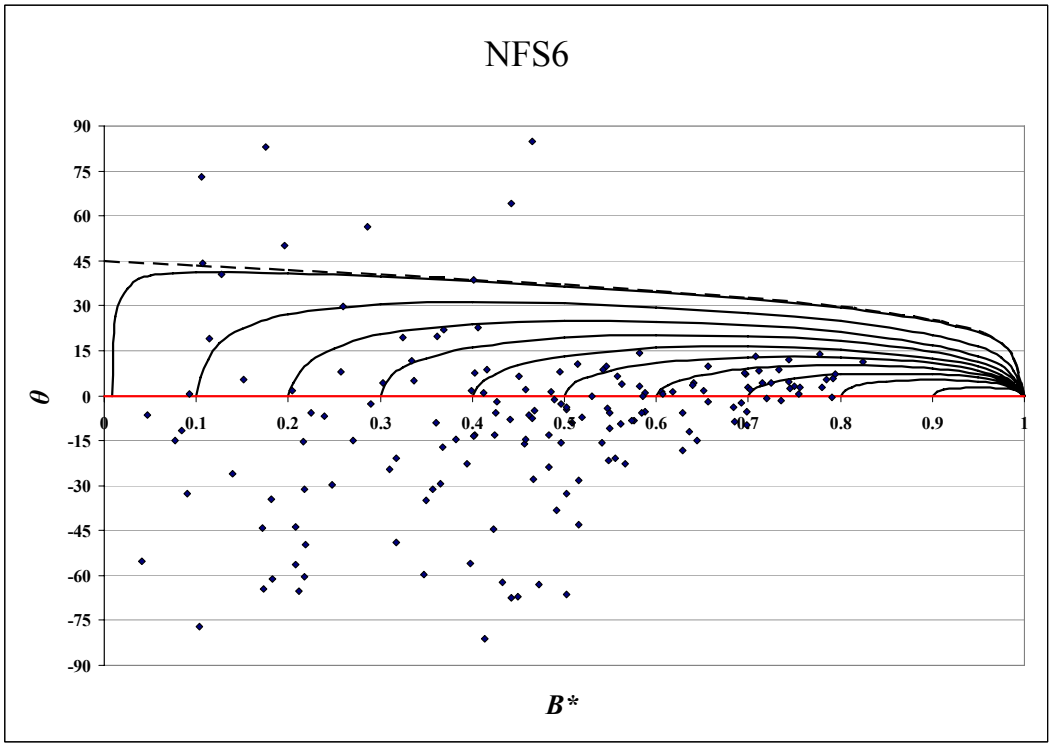

Figure 29: (see caption for Fig. 10)

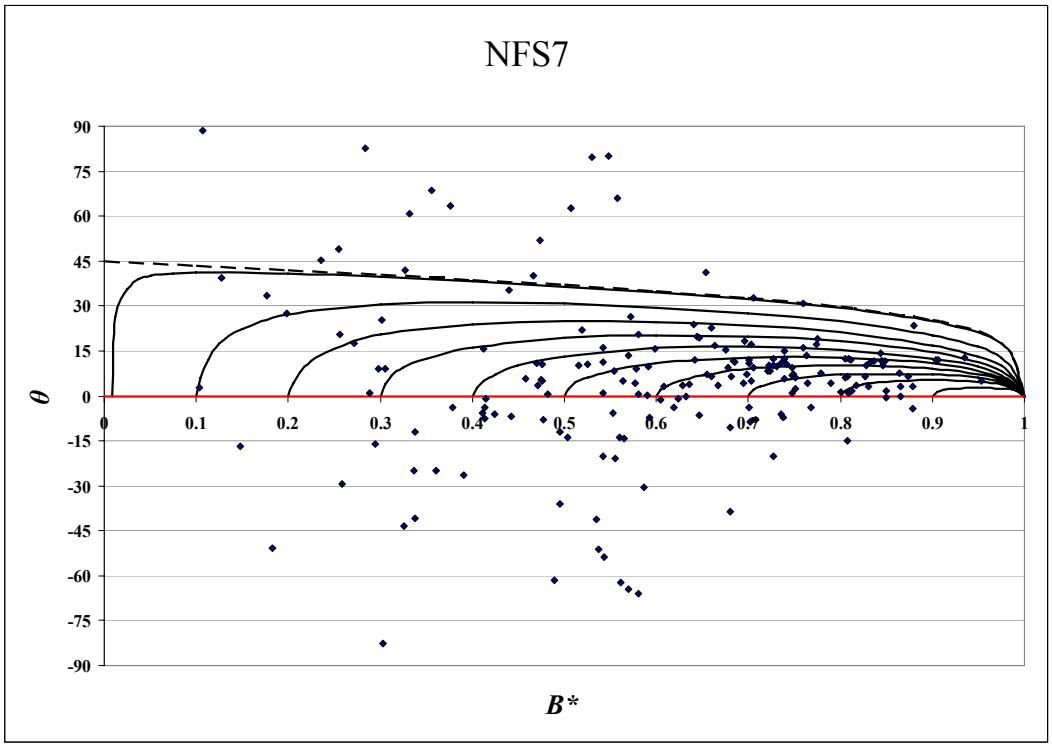

Figure 30: (see caption for Fig. 10)

Summary and Conclusions

In this thesis, two methods were introduced for extracting quantitative information about the kinematics of flow in shear zones. These methods were applied to mylonites from the Sandhill Corner Mylonite Zone, a strand of the Norumbega Fault System, and a discrepancy was noted between the results of each method. Numerical modeling experiments were conducted and, assuming a low-viscosity layer was present between porphyroclasts and the rock matrix, the discrepancy was resolved.

This thesis also introduced a new tool, the 'high strain paleoviscometer', for extracting paleo-viscosity contrasts in mylonites and other high strain tectonites. Even if a low-viscosity layer surrounding clasts does not accurately represent the true slip condition at their margins, other mechanisms, such as imperfect bonding between clast margins and minerals in the matrix, conceivably could result in similar rotational behavior. The actual mechanism that affected clasts in SCMZ mylonites is not yet apparent.

Feldspar porphyroclasts were chosen for analysis at the onset of this study because they are abundant in SCMZ mylonites. Future studies could examine the SPO fabrics of mica 'fish', a type of porphyroclast consisting of mica that exhibit parallelepiped shapes. Parallelograms are no more difficult to design in 2-D *COMSOL* models than are ellipses, so ongoing modeling efforts could target these shapes. Preliminary work by Johnson and Lenferink (in preparation) suggests imperfect viscous coupling between mica fish and the rock matrix in SCMZ mylonites may correlate positively with bulk mica content.

The general conclusions of this thesis are: (1) the rotated porphyroclast method of kinematic vorticity analysis is not robust because strain localization at clast margins gives rise to markedly different SPO fabrics, causing W_m values inferred from B_{crit} to appear low; (2) it may be possible to estimate $\tilde{\eta}$ in clast-bearing mylonites, but quantitative measurements are limited by noise in SPO fabrics (due to clast interaction and other mechanisms that effect inhomogeneous flow patterns).

References

Bretherton, F.P. 1962. The motion of rigid particles in shear flow at low Reynolds number. *J. Fluid. Mech.* 14, 284–301.

COMSOL AB. COMSOL Multiphysics Quick Start and Quick Reference. Stockholm, Sweden, 2006. <http://www.comsol.com>

Einstein, A. 1906. Eine neue Bestimmung der Moleküldimensionen. *Annalen der Physik* 19, 289–306.

Gerbi, C., and West, D.P., Jr. In review. Tectonothermal coupling in an evolving compressional-transpressional system: An example from the Acadian Orogen in Maine. *Geol. Soc. Am. Bull*.

Ghosh, S.K., Ramberg, H. 1976. Reorientation of inclusions by combination of pure shear and simple shear. *Tectonophysics* 34, 1–70.

Grover, T.W., Fernandes, L.C. 2003. Bedrock geology of the Weeks Mills 7.5' quadrangle, Maine. Maine Geological Survey Open-File Map 03-49, Scale 1:24,000.

Hubbard, M.S., Wang, H. 1999. Temperature variability during shear deformation: An interpretation of microstructures along the central Norumbega fault zone, Maine. In: Ludman, A., West, D.P., Jr. (Eds). Norumbega Fault System of the Northern Appalachians. *Geol. Soc. Am. Spec. Pap.* 331, 25–40.

Iacopini, D., Passchier, C.W., Koehn, D., Carosi, R. 2007. Fabric attractors in general triclinic flow systems and their application to high strain shear zones: A dynamical system approach. *J. Struct. Geol.* 29, 298–317.

Ildefonse, B., Mancktelow, N.S. 1992. Mechanical interactions between rigid particles in a deforming ductile matrix. Analogue experiments in simple shear flow. *J. Struct. Geol.* 14, 1253–1266.

Ildefonse, B., Mancktelow, N.S. 1993. Deformation around rigid particles: the influence of slip at the particle/matrix interface. *Tectonophysics* 221, 345–359.

Jeffery, G.B. 1922. The motion of ellipsoidal particles immersed in a viscous fluid. *Proc. Roy. Soc. Lon. Ser. A* 102, 161–179.

Jessell, M., Lister, G.S. 1990. A simulation of the temperature dependence fabrics of quartz. In: Knipe, R.J., Rutter, E.H. (Eds). Deformation Mechanisms, Rheology and Tectonics. *Geol. Soc., Lon. Spec. Pub.* 54, 353–362.

Jessup, M.J., Law, R.D., Frassi, C. 2007. The Rigid Grain Net (RGN): an alternative method for estimating kinematic vorticity number (W_m). *J. Struct. Geol.* 29, 411–421.

Jezek, J., Saic, S., Segeth, K. 1999. Numerical modeling of the movement of a rigid particle in viscous fluid. *Appl. Math.* 6, 469–479.

Johnson, S.E. 2008. Numerical investigation of the effects of strain localization on rigid object kinematics. In: Bons, P.D.D., Koehn, D., Jessell, M.W. (Eds). Microdynamics Simulation, Lecture Notes in Earth Science, v. 106.

Lapworth, C. 1885. The highland controversy in British geology: its causes, courses, and consequences. *Nature* 32, 558–559.

Law, R.D., Searle, M.P., Simpson, R.L. 2004. Strain, deformation temperatures and vorticity of flow at the top of the Greater Himalayan Slab, Everest Massif, Tibet. *J. Geol. Soc. London.* 161, 305–320.

Lister, G.S., Hobbs, B.E. 1980. The simulation of fabric development during plastic deformation and its application to quartzite: the influence of deformation history. *J. Struct. Geol.*, 2 355–370.

Ludman, A., West, D.P., Jr. (Eds). Norumbega Fault System of the Northern Appalachians. *Geol. Soc. Am. Spec. Pap.* 331, 25–40.

Mancktelow, N.S., Arbaret, L., Pennacchioni, G. 2002. Experimental observations on the effect of interface slip on rotation and stabilization of rigid particles in simple shear and a comparison with natural mylonites. *J. Struct. Geol.* 24, 567–585.

Marques, F.O., Bose, S. 2004. Influence of a permanent low-friction boundary on rotation and in rigid inclusions/viscous matrix systems from an analogue perspective. *Tectonophysics* 382, 229–245.

McKenzie, D. 1979. Finite deformation during fluid flow. *Geophys. J. R. astr. Soc.* 58, 689–715.

Means, W.D., Hobbs, B.E., Lister, G.S., Williams, P.F. 1980. Vorticity and non-coaxiality in progressive deformation. *J. Struct. Geol.* 2, 371–378.

Osberg, P.H., Hussey, A.M., II, Boone, G.M. (Eds). 1985. Bedrock Geologic Map of Maine. Maine Geological Survey Map, Scale 1:500,000.

Passchier, C.W. 1987. Stable positions of rigid objects in non-coaxial flow – a study in vorticity analysis. *J. Struct. Geol.* 9, 679–690.

Passchier, C.W. 1988a. Analysis of deformational paths in shear zones. *Geol. Rdsch.* 77, 309–318.

Passchier, C.W. 1988b. The use of Mohr circles to describe non-coaxial flow – a study in vorticity analysis. *Tectonophysics* 149, 323–338.

Passchier, C.W., Sokoutis, D. 1993. Experimental modeling of mantled porphyroclasts. *J. Struct. Geol.* 15, 895–909.

Passchier, C.W., Trouw, R.A.J. 2005. Microtectonics. Springer, 2nd Ed., 366 pp.

Passchier, C.W., Urai, J.L. 1988. Vorticity and strain analysis using Mohr diagrams. *J. Struct. Geol.* 10, 755–763.

Pennachioni, G., Di Toro, G., Mancktelow, N.S. 2000. Strain-insensitive preferred orientation of porphyroclasts in Mont Mary mylonite. *J. Struct. Geol.* 23, 1281–1298.

Schmid, S.M., Casey, M. 1986. Complete fabric analysis of some commonly observed quartz *c*-axis patterns. In: Hobbs, B.E., Heard, H.C. (Eds). Mineral and rock deformation: Laboratory studies. *Am. Geophys. Union. Geophys. Monogr.* 36, 263–286

Schmid, D.W., Podladshikov, Y.Y. 2005. Mantled porphyroclast gauges. *J. Struct. Geol.* 27, 571–585.

Simpson, C., De Paor, D.G., 1993. Strain and kinematic analysis in general shear zones. *J. Struct. Geol.* 15, 1–20.

Takeshita, T., Wenk, H.R. & Lebensohn, R. 1999. Development of preferred orientation and microstructure in sheared quartzite: comparison of natural data and simulated results. *Tectonophysics* 312, 133–155.

Ten Brink, C.E., Passchier, C.W., 1995. Modelling of mantled porphyroclasts using non-Newtonian rock analogue materials. *J. Struct. Geol.* 17, 131–146.

Ten Gruitenhuis, S.M., Passcier, C.W., Bons, P.D. 2002. The influence of strain localization on the rotation behaviour of rigid objects in experimental shear zones. *J. Struct. Geol.* 24, 485–499.

Tikoff, B., Fossen, H. 1995. The limitations of three-dimensional kinematic vorticity analysis. *J Struct. Geol.* 17, 1771–1784.

Truesdell, C. 1953. Two measures of vorticity. *J. Rational Mech. Anal.* 2, 173–217.

Tucker, R.D., Osberg, P.H., Berry, H.N., IV. 2001. The geology of a part of Acadia and the nature of the Acadian orogeny across central and eastern Maine. *Am. J. Sci.* 301, 205–260.

Tullis, J.,1977. Preferred orientation of quartz produced by slip during plane strain. Tectonophysics, 39, 87–102.

Tullis, J., Christie, J.M., Griggs, D.T. 1973. Microstructures and preferred orientations of experimentally deformed quartzites. *Bull. Geol. Soc. Am.* 84, 297–314.

Wallis, S.R. 1992. Vorticity analysis in a metachert from the Sanbagawa Belt, SW Japan. *J. Struct. Geol.* 14, 271–280.

Wallis, S.R. 1995. Vorticity analysis and recognition of ductile extension in the Sanbagawa belt, SW Japan. *J. Struct. Geol.* 17, 1077–1093.

Wenk, H.-R., Canova, G., Molinari, A., Kocks, U.F. 1989. Viscoelastic modeling of texture development in quartzite. *J. Geophys. Res.* 94, 895-906.

West, D.P., Jr. 1999. Timing of displacements along the Norumbega fault system, southcentral and south-coastal Maine. In: Ludman, A., West, D.P., Jr. (Eds). Norumbega Fault System of the Northern Appalachians. *Geol. Soc. Am. Spec. Pap.* 331, 167–178.

West, D.P., Jr., Barnard, N. Gerbi, C. 2006. Metamorphosed iron-rich rocks in southcentral Maine: From peri-Gondwanan sedimentation through Acadian metamorphism. Geological Society of America Abstracts with Program, vol. 38, 7, p. 48.

West, D.P., Jr., Guidotti, C.V., Lux, D.R. 1995. Silurian orogenesis in the western Penobscot Bay region, Maine. *Can. J. Earth Sci.* 32, 1845–1858.

West, D.P., Jr., Lux, D.R. 1993. Direct dating of mylonitization by the $^{40}Ar/^{39}Ar$ method: An example from the Norumbega fault zone, Maine. *Earth. Planet. Sc. Lett.* 120, 221–237.

West, D.P., Jr., Lux, D.R., Hussey, A.M., II. 1988. $^{40}Ar/^{39}Ar$ hornblende ages from southwestern Maine: Evidence for Late Paleozoic metamorphism. *Atlantic Geol.* 24, 225–240.

West, D.P., Jr., Peterman, E.M. 2004. Bedrock geology of the Razorville 7.5' quadrangle, Maine. Maine Geological Survey Map 04-29, Scale 1:24,000.

Xypolias, P., Koukouvelas, I.K. 2001. Kinematic vorticity and strain rate patterns associated with ductile extrusion in the Chelmos Shear Zone (External Hellenides, Greece). *Tectonophysics* 338, 59–77.

Nomenclature

$\boldsymbol{v}$	m s^{-1}	velocity field (components u, v, w)
$\mathbf{V}$	s^{-1}	velocity gradient tensor
$\mathbf{E}$	s^{-1}	strain rate tensor
$\mathbf{\Omega}$	s^{-1}	vorticity tensor
S	s^{-1}	shear strain rate in xy-plane
W	s^{-1}	vorticity in xy-plane
s_r	-	ratio of rate of pure shearing to rate of simple shearing
W_k	-	kinematic vorticity number
$\hat{s}_i$	-	instantaneous stretching axes (ISA_1, ISA_2, ISA_3)
$\hat{l}_i$	-	flow apophyses (AP_1, AP_2, AP_3)
R	-	aspect ratio of clast
B	-	shape factor of clast
B'	-	lineation-parallel shape
α	-	acute angle between flow apophyses
β	-	acute angle between ISA_1 and AP_1
δ	-	acute angle between foliation and AP_1
θ	-	acute angle between foliation and stable clast orientation
$\widetilde{\eta}$	-	ratio of lubricant viscosity to matrix viscosity (a.k.a. viscosity contrast)

Appendices

1. *Instantaneous flow*

In a fixed external reference frame, the velocity field $\boldsymbol{v}$ that describes a continuous medium undergoing steady, monoclinic, plane-strain deformation is the product of the velocity gradient tensor **V** and the position vector $\boldsymbol{r}$:

$$\begin{pmatrix} u \\ v \\ w \end{pmatrix} = \begin{pmatrix} \frac{\partial u}{\partial x} & \frac{\partial u}{\partial y} & \frac{\partial u}{\partial z} \\ \frac{\partial v}{\partial x} & \frac{\partial v}{\partial y} & \frac{\partial v}{\partial z} \\ \frac{\partial w}{\partial x} & \frac{\partial w}{\partial y} & \frac{\partial w}{\partial z} \end{pmatrix} \begin{pmatrix} x \\ y \\ z \end{pmatrix} = \begin{pmatrix} 0 & \frac{S-W}{2} & 0 \\ \frac{S+W}{2} & 0 & 0 \\ 0 & 0 & 0 \end{pmatrix} \begin{pmatrix} x \\ y \\ z \end{pmatrix}$$

Here S is the shear strain rate and W is the vorticity in the xy-plane, defined as:

$$S = \frac{\partial v}{\partial x} + \frac{\partial u}{\partial y}$$

$$W = \frac{\partial v}{\partial x} - \frac{\partial u}{\partial y}$$

The symmetric part of **V** is the strain rate tensor **E**:

$$E_{ij} = \frac{1}{2}(V_{ij} + V_{ij}^{\mathrm{T}}) \qquad \mathbf{E} = \begin{pmatrix} 0 & \frac{S}{2} & 0 \\ \frac{S}{2} & 0 & 0 \\ 0 & 0 & 0 \end{pmatrix}$$

The antisymmetric part of **V** is the vorticity tensor **Ω**:

$$\Omega_{ij} = \frac{1}{2}(V_{ij} - V_{ij}^{\mathrm{T}}) \qquad \mathbf{\Omega} = \begin{pmatrix} 0 & -\frac{W}{2} & 0 \\ \frac{W}{2} & 0 & 0 \\ 0 & 0 & 0 \end{pmatrix}$$

The radial component of the velocity field is

$$v_r = \boldsymbol{v} \cdot \hat{r} = \left\{ \begin{pmatrix} 0 & \frac{S-W}{2} & 0 \\ \frac{S+W}{2} & 0 & 0 \\ 0 & 0 & 0 \end{pmatrix} \begin{pmatrix} x \\ y \\ z \end{pmatrix} \right\} \cdot \left\{ \frac{1}{\sqrt{x^2+y^2}} \begin{pmatrix} x \\ y \\ z \end{pmatrix} \right\}$$

$$= \frac{xy}{\sqrt{x^2+y^2}} \left(\frac{S-W}{2} + \frac{S+W}{2} \right)$$

$$\dot{\gamma}_r(\psi) = \frac{v_r}{r} = S\cos(\psi)\sin(\psi) = \frac{S}{2}\sin(2\psi)$$

Here ψ is measured from the x-axis toward the y-axis. The instantaneous stretching axes are at $\psi = \pm 45°$ (the orientations at which the magnitude of $\dot{\gamma}_r$ is greatest). The circumferential component of the field is

$$v_\psi = \boldsymbol{v} \cdot \hat{\psi} = \left\{ \begin{pmatrix} 0 & \frac{S-W}{2} & 0 \\ \frac{S+W}{2} & 0 & 0 \\ 0 & 0 & 0 \end{pmatrix} \begin{pmatrix} x \\ y \\ z \end{pmatrix} \right\} \cdot \left\{ \frac{1}{\sqrt{x^2+y^2}} \begin{pmatrix} -y \\ x \\ 0 \end{pmatrix} \right\}$$

$$= \frac{1}{\sqrt{x^2+y^2}} \left(\frac{S+W}{2}x^2 - \frac{S-W}{2}y^2 \right)$$

$$\omega(\psi) = \frac{v_\psi}{r} = \frac{S+W}{2}\cos^2(\psi) - \frac{S-W}{2}\sin^2(\psi) = \frac{W}{2} + \frac{S}{2}\cos(2\psi)$$

Rotation of material lines and planes ceases as $2\psi \rightarrow \alpha$ (the angle between the velocity field eigenvectors or 'flow apophyses'; Fig. 4):

$$\alpha = 2\cos^{-1}\left(\sqrt{\frac{S-W}{2S}}\right) = \cos^{-1}\left|\frac{W}{S}\right|$$

For plane-strain deformation, the kinematic vorticity number W_k (Truesdell, 1953) is the ratio of vorticity to strain rate in the *xy*-plane:

$$W_k = \sqrt{\left|\frac{\text{tr}\,\mathbf{\Omega}^2}{\text{tr}\,\mathbf{E}^2}\right|} = \left|\frac{W}{S}\right| = \left|\frac{S-W}{S}\right| - \frac{S}{S} = 2\cos^2(\frac{\alpha}{2}) - 1 = \cos(\alpha)$$

For steady monoclinic deformation, three flow types are possible: pure shear, simple shear, and general non-coaxial shear. The two former types comprise the end members of which the latter is intermediate, encompassing a spectrum of flow types. W_k quantifies the non-coaxiality of flow, ranging from 0 for pure shear to 1 for simple shear.

In analog experiments, one typically controls the pure and simple shear components of deformation, so it is convenient to define the pure-to-simple strain rate ratio s_r as a measure of non-coaxiality (Ghosh and Ramberg, 1976). W_k and s_r are related as follows:

$$s_r = \frac{\dot{\varepsilon}}{\dot{\gamma}} = \frac{S\sin(\alpha)}{2W} = \frac{\sqrt{1-W_k^2}}{2W_k}$$

2. *Finite strain*

The eigenvalues and eigenvectors of **V** are

$$\begin{vmatrix} -\mu & \frac{S-W}{2} & 0 \\ \frac{S+W}{2} & -\mu & 0 \\ 0 & 0 & -\mu \end{vmatrix} = 0$$

$$\mu^3 - \frac{\mu S^2}{4} + \frac{\mu W^2}{4} = 0$$

$$\mu_1 = \frac{\sqrt{S^2-W^2}}{2},\ \mu_2 = -\frac{\sqrt{S^2-W^2}}{2},\ \mu_3 = 0$$

$$\hat{l}_1 = \frac{1}{\sqrt{2S}}\begin{pmatrix}\sqrt{S-W}\\ \sqrt{S+W}\\ 0\end{pmatrix},\ \hat{l}_2 = \frac{1}{\sqrt{2S}}\begin{pmatrix}\sqrt{S-W}\\ -\sqrt{S+W}\\ 0\end{pmatrix},\ \hat{l}_3 = \begin{pmatrix}0\\0\\1\end{pmatrix}$$

Here $\hat{l}_1$, $\hat{l}_2$, and $\hat{l}_3$ correspond to the flow apophyses, which are identical to the instantaneous stretching axes $\hat{s}_1$, $\hat{s}_2$, and $\hat{s}_3$ in the case of pure shear (for simple shear, the flow apophyses vanish). Substituting *p*

$= \sqrt{S - W}$ and $q = \sqrt{S + W}$ and separating variables, the velocity field may be rewritten and solved as functions of time:

$$\begin{pmatrix} u' \\ v' \\ w' \end{pmatrix} = \begin{pmatrix} \mu_1 & 0 & 0 \\ 0 & \mu_2 & 0 \\ 0 & 0 & \mu_3 \end{pmatrix} \begin{pmatrix} x' \\ y' \\ z' \end{pmatrix} = \begin{pmatrix} \frac{pq}{2} & 0 & 0 \\ 0 & -\frac{pq}{2} & 0 \\ 0 & 0 & 0 \end{pmatrix} \begin{pmatrix} x' \\ y' \\ z' \end{pmatrix}$$

$$x'(t) = c_1 \, e^{pqt/2}$$
$$y'(t) = c_2 \, e^{-pqt/2}$$
$$z'(t) = c_3$$

$$\begin{pmatrix} x \\ y \\ z \end{pmatrix} = \frac{c_1}{\sqrt{2S}} \begin{pmatrix} p \\ q \\ 0 \end{pmatrix} e^{pqt/2} + \frac{c_2}{\sqrt{2S}} \begin{pmatrix} p \\ -q \\ 0 \end{pmatrix} e^{-pqt/2} + c_3 \begin{pmatrix} 0 \\ 0 \\ 1 \end{pmatrix}$$

The constants of integration correspond to the initial conditions $x = x_o$, $y = y_o$, and $z = z_o$:

$$c_1 = \sqrt{\frac{S}{2}} \left(\frac{x_o}{p} + \frac{y_o}{q} \right)$$
$$c_2 = \sqrt{\frac{S}{2}} \left(\frac{x_o}{p} - \frac{y_o}{q} \right)$$
$$c_3 = z_o$$

$$\begin{pmatrix} x \\ y \\ z \end{pmatrix} = \frac{1}{2} \left(\frac{x_o}{p} + \frac{y_o}{q} \right) \begin{pmatrix} p \\ q \\ 0 \end{pmatrix} e^{pqt/2} + \frac{1}{2} \left(\frac{x_o}{p} - \frac{y_o}{q} \right) \begin{pmatrix} p \\ -q \\ 0 \end{pmatrix} e^{-pqt/2} + z_o \begin{pmatrix} 0 \\ 0 \\ 1 \end{pmatrix}$$

$$= \begin{pmatrix} 0 \\ 0 \\ z_o \end{pmatrix} + \begin{pmatrix} x_o \\ y_o \\ 0 \end{pmatrix} \cosh\left(\frac{pqt}{2}\right) + \frac{1}{pq} \begin{pmatrix} p^2 y_o \\ q^2 x_o \\ 0 \end{pmatrix} \sinh\left(\frac{pqt}{2}\right) + \begin{pmatrix} 0 \\ 0 \\ z_o \end{pmatrix}$$

$$= \begin{pmatrix} \cosh\left(\frac{pqt}{2}\right) & \frac{p}{q}\sinh\left(\frac{pqt}{2}\right) & 0 \\ \frac{q}{p}\sinh\left(\frac{pqt}{2}\right) & \cosh\left(\frac{pqt}{2}\right) & 0 \\ 0 & 0 & 1 \end{pmatrix} \begin{pmatrix} x_o \\ y_o \\ z_o \end{pmatrix}$$

The finite strain tensor may be written in terms of the kinematic vorticity number W_k:

$$F_{ij} = \begin{pmatrix} \cosh(\frac{\sqrt{1-W_k^2}}{2}St) & \frac{1+W_k}{\sqrt{1-W_k^2}}\sinh(\frac{\sqrt{1-W_k^2}}{2}St) & 0 \\ \frac{1-W_k}{\sqrt{1-W_k^2}}\sinh(\frac{\sqrt{1-W_k^2}}{2}St) & \cosh(\frac{\sqrt{1-W_k^2}}{2}St) & 0 \\ 0 & 0 & 1 \end{pmatrix}, \qquad 0 < W_k < 1$$

$$= \begin{pmatrix} 1 & St & 0 \\ 0 & 1 & 0 \\ 0 & 0 & 1 \end{pmatrix}, \qquad W_k = 1$$

These equations require modification for flow types involving a change in area (*i.e.*, departure from plane-strain conditions; Passchier, 1988a,b).